

Deleted: Interpretation of

Deleted: in relation

Deleted: and seasonality

1 **Relating geostationary satellite measurements of aerosol optical**  
2 **depth (AOD) over East Asia to fine particulate matter (PM<sub>2.5</sub>):**  
3 **insights from the KORUS-AQ aircraft campaign and GEOS-**  
4 **Chem model simulations**

5 Shixian Zhai<sup>1</sup>, Daniel J. Jacob<sup>1</sup>, Jared F. Brewer<sup>1</sup>, Ke Li<sup>1</sup>, Jonathan M. Moch<sup>1</sup>, Jhoon Kim<sup>2,3</sup>,  
6 Seoyoung Lee<sup>2</sup>, Hyunkwang Lim<sup>2</sup>, Hyun Chul Lee<sup>3</sup>, Su Keun Kuk<sup>3</sup>, Rokjin J. Park<sup>4</sup>, Jaemin I.  
7 Jeong<sup>4</sup>, Xuan Wang<sup>5</sup>, Pengfei Liu<sup>6</sup>, Gan Luo<sup>7</sup>, Fangqun Yu<sup>7</sup>, Jun Meng<sup>8, a</sup>, Randall V. Martin<sup>8</sup>,  
8 Katherine R. Travis<sup>9</sup>, Johnathan W. Hair<sup>9</sup>, Bruce E. Anderson<sup>9</sup>, Jack E. Dibb<sup>10</sup>, Jose L.  
9 Jimenez<sup>11</sup>, Pedro Campuzano-Jost<sup>11</sup>, Benjamin A. Nault<sup>11, b</sup>, Jung-Hun Woo<sup>12</sup>, Younha Kim<sup>13</sup>,  
10 Qiang Zhang<sup>14</sup>, Hong Liao<sup>15</sup>

11 <sup>1</sup>Harvard John A. Paulson School of Engineering and Applied Sciences, Harvard University, Cambridge, MA, USA

12 <sup>2</sup>Department of Atmospheric Sciences, Yonsei University, Seoul, Republic of Korea

13 <sup>3</sup>Samsung Particulate Matter Research Institute, Samsung Advanced Institute of Technology, 130 Samsung-ro,  
14 Yeongtong-gu, Suwon-si, Gyeonggi-do, Republic of Korea

15 <sup>4</sup>School of Earth and Environmental Sciences, Seoul National University, Seoul, Republic of Korea

16 <sup>5</sup>School of Energy and Environment, City University of Hong Kong, Hong Kong SAR, China

17 <sup>6</sup>School of Earth and Atmospheric Sciences, Georgia Institute of Technology, Atlanta, GA, USA

18 <sup>7</sup>Atmospheric Sciences Research Center, University at Albany, Albany, New York, USA

19 <sup>8</sup>Department of Energy, Environmental & Chemical Engineering, Washington University in St Louis, MO, USA

20 <sup>9</sup>NASA Langley Research Center, Hampton, VA, USA

21 <sup>10</sup>Institute for the Study of Earth, Oceans, and Space, University of New Hampshire, Durham, NH, USA

22 <sup>11</sup>Department of Chemistry, and Cooperative Institute for Research in Environmental Sciences, University of  
23 Colorado, Boulder, CO, USA

24 <sup>12</sup>Department of Civil and Environmental Engineering, Konkuk University, Seoul, Republic of Korea

25 <sup>13</sup>International Institute for Applied Systems Analysis (IIASA), 2361 Laxenburg, Austria

26 <sup>14</sup>Department of Earth System Science, Tsinghua University, Beijing, China.

27 <sup>15</sup>Jiangsu Key Laboratory of Atmospheric Environment Monitoring and Pollution Control, Collaborative Innovation  
28 Center of Atmospheric Environment and Equipment Technology, School of Environmental Science and  
29 Engineering, Nanjing University of Information Science and Technology, Nanjing, China.

30 <sup>a</sup> Now at Department of Atmospheric & Oceanic Sciences, University of California, Los Angeles, California, USA

31 <sup>b</sup> Now at Center for Aerosol and Cloud Chemistry, Aerodyne Research, Inc., Billerica, MA, USA

32 *Correspondence:* Shixian Zhai (zhaisx@g.harvard.edu)

33

37 **Abstract.** Geostationary satellite measurements of aerosol optical depth (AOD) over East Asia from the GOCI and  
38 AHI instruments can augment surface monitoring of fine particulate matter (PM<sub>2.5</sub>) air quality, but this requires  
39 better understanding of the AOD-PM<sub>2.5</sub> relationship. Here we use the GEOS-Chem chemical transport model to  
40 analyze the critical variables determining the AOD-PM<sub>2.5</sub> relationship over East Asia by simulation of observations  
41 from satellite, aircraft, and ground-based datasets. This includes the detailed vertical aerosol profiling over South  
42 Korea from the KORUS-AQ aircraft campaign (May-June 2016) with concurrent ground-based PM<sub>2.5</sub> composition,  
43 PM<sub>10</sub>, and AERONET AOD measurements. The KORUS-AQ data show that 550 nm AOD is mainly contributed by  
44 sulfate-nitrate-ammonium (SNA) and organic aerosols in the planetary boundary layer (PBL), despite large dust  
45 concentrations in the free troposphere, reflecting the optically effective size and high hygroscopicity of the PBL  
46 aerosols. We updated SNA and organic aerosol size distributions in GEOS-Chem to represent aerosol optical  
47 properties over East Asia by using in-situ measurements of particle size distributions from KORUS-AQ. We find  
48 that SNA and organic aerosols over East Asia have larger size (number median radius of 0.11 μm with geometric  
49 standard deviation of 1.4) and 20% larger mass extinction efficiency as compared to North America (default setting  
50 in GEOS-Chem). Although GEOS-Chem is successful in reproducing the KORUS-AQ vertical profiles of aerosol  
51 mass, its ability to link AOD to PM<sub>2.5</sub> is limited by under-accounting of coarse PM and by a large overestimate of  
52 nighttime PM<sub>2.5</sub> nitrate. The GOCI/AHI AOD data over East Asia in different seasons show agreement with  
53 AERONET AODs and a spatial distribution consistent with surface PM<sub>2.5</sub> network data. The AOD observations over  
54 North China show a summer maximum and winter minimum, opposite in phase to surface PM<sub>2.5</sub>. This is due to low  
55 PBL depths compounded by high residential coal emissions in winter, and high relative humidity (RH) in summer.  
56 Seasonality of AOD and PM<sub>2.5</sub> over South Korea is much weaker, reflecting weaker variation of PBL depth and lack  
57 of residential coal emissions.

## 58 1 Introduction

59 PM<sub>2.5</sub> (particulate matter with aerodynamic diameter less than 2.5 μm) in surface air is a severe public health  
60 concern in East Asia, but surface monitoring networks are too sparse to thoroughly assess population exposure.  
61 Satellite observations of aerosol optical depth (AOD) can provide a valuable complement (Van Donkelaar et al.,  
62 2015). Geostationary satellite sensors, including the Geostationary Ocean Color Imager (GOCI) launched by the  
63 Korea Aerospace Research Institute (KARI) in 2011 (Choi et al., 2016, 2018, 2019) and the Advanced Himawari  
64 Imager (AHI) launched by the Japanese Meteorological Agency (JMA) in 2014 (Lim et al., 2018, 2021), offer the  
65 potential for high-density mapping of PM<sub>2.5</sub> over East Asia. However, more confidence is needed in relating AOD to  
66 PM<sub>2.5</sub>. Here we evaluate the capability of the GEOS-Chem chemical transport model (CTM) to simulate AOD-PM<sub>2.5</sub>  
67 relationships over East Asia, exploiting in-situ aircraft measurements of vertical aerosol profiles and optical  
68 properties from the joint NASA-NIER Korea - United States Air Quality (KORUS-AQ) field study in May-June  
69 2016 (Crawford et al., 2021; Peterson et al., 2019; Jordan et al., 2020) together with GOCI/AHI geostationary  
70 satellite data and surface measurement networks. This enables us to identify critical variables and uncertainties for  
71 inferring PM<sub>2.5</sub> from satellite AOD data.

Deleted: S

Deleted: of PM<sub>2.5</sub>

Deleted: and

Deleted: s

Deleted: , including the

Deleted: ()

Deleted: AX

Deleted: use

Deleted: analyze and

Deleted: the

Deleted: as well as

Deleted: compared to

Deleted: observation

85 A number of past studies have used satellite AOD data to infer surface PM<sub>2.5</sub> using physical and statistical models.  
86 The standard geophysical approach has been to use a CTM, such as GEOS-Chem, to compute the PM<sub>2.5</sub>/AOD ratio  
87 (Liu et al., 2004; van Donkelaar et al., 2006; van Donkelaar et al., 2015; Xu et al., 2015; Geng et al., 2017), with  
88 recent applications correcting for CTM biases using available PM<sub>2.5</sub> surface network data (Brauer et al., 2016; Van  
89 Donkelaar et al., 2016; van Donkelaar et al., 2019; Hammer et al., 2020). An alternative approach is to use machine-  
90 learning algorithms to relate satellite AOD to PM<sub>2.5</sub> by training on the surface network data (Hu et al., 2017; Chen et  
91 al., 2018; Xiao et al., 2018; Wei et al., 2021; Pendergrass et al., 2021), and sometimes including CTM values as  
92 predictors (Di et al., 2019; Xue et al., 2019). Yet another approach is to assimilate the satellite-measured AODs in a  
93 CTM and correct in this manner the PM<sub>2.5</sub> simulation, although this requires attribution of model AOD errors to  
94 specific model parameters (Kumar et al., 2019; Saide et al., 2014; Sekiyama et al., 2010; Cheng et al., 2019). In all  
95 of these approaches, a better physical understanding of the AOD-PM<sub>2.5</sub> relationship as simulated by CTMs can  
96 greatly enhance the capability to infer PM<sub>2.5</sub> from AOD data.

Deleted: physical relationship of

97 AOD measures aerosol extinction (scattering and absorption) integrated over the atmospheric column, so that its  
98 relationship to 24-hr average surface PM<sub>2.5</sub> (the standard air quality metric) depends on the aerosol vertical  
99 distribution and optical properties, ambient relative humidity (RH), diurnal variation of PM<sub>2.5</sub>, and contribution from  
100 coarse particulate matter to AOD. Little study of these factors has been conducted for East Asia. Airborne  
101 measurements of aerosol vertical profiles in East Asia are very limited (Liu et al., 2009; Sun et al., 2013). AOD is  
102 highly sensitive to RH (Brock et al., 2016; Latimer and Martin et al., 2019; Saide et al., 2020), but the impact from  
103 RH uncertainty on AOD simulation lacks evaluation. In addition, because the AOD is a daytime measurement that  
104 needs to be related to 24-h average PM<sub>2.5</sub>, the diurnal variation of PM<sub>2.5</sub> needs to be understood (Guo et al., 2017;  
105 Lennartson et al., 2018). Finally, there has been to our knowledge no study of how coarse anthropogenic PM may  
106 contribute to the AOD measurements. Coarse anthropogenic PM (distinct from desert dust) is known to be high over  
107 East Asia (Chen et al., 2015; Dai et al., 2018).

## 108 2 Data and methods

### 109 2.1 Observations

110 We use observations over China and South Korea from multiple platforms including surface sites, aircraft, and  
111 satellites (Table 1 and 2). Surface data (Table 1) include PM<sub>2.5</sub> from national observation networks in China (Zhai et  
112 al., 2019) and South Korea (Jordan et al., 2020), speciated PM<sub>2.5</sub> at 7 supersites in South Korea during KORUS-AQ  
113 (Choi et al., 2019), and ground-based AODs from the AERONET network at 5 sites in North China and 10 sites in  
114 South Korea (21 sites during KORUS-AQ). We use total and fine-mode AODs at 500 nm wavelength from the  
115 AERONET Version 3; Spectral Deconvolution Algorithm (SDA) Version 4.1 Retrieval Level 2.0 database (Giles et  
116 al., 2019; O'Neill et al., 2003). The AERONET AODs at 500 nm are converted to 550 nm using total and fine mode  
117 Ångström Exponents at 500 nm for consistency with the satellite AOD data.

Deleted: 2

Deleted: Level 2.0

121 **Table 1. Surface site observations used in this work (2016)**

Variable	Number of sites
PM <sub>2.5</sub> in North China <sup>a</sup>	117
PM <sub>2.5</sub> in South Korea <sup>b</sup>	130
PM <sub>2.5</sub> composition in South Korea (May-June 2016) <sup>c</sup>	7
AERONET total and fine mode AOD in North China <sup>d</sup>	5
AERONET total and fine mode AOD in South Korea <sup>d</sup>	10-21 <sup>e</sup>

122 <sup>a</sup> Hourly PM<sub>2.5</sub> from the China National Environmental Monitoring Centre (CNEMC; [quotsoft.net/air/](http://soft.net/air/)) in North  
 123 China (115.5-122° E, 34.5-40.5° N), including only sites with more than 90% data coverage in each month of 2016.  
 124 Quality control of the CNEMC dataset is described in our previous study (Zhai et al., 2019). The PM<sub>2.5</sub>  
 125 measurements are made at reference RH ≤ 35%.

126 <sup>b</sup> Hourly PM<sub>2.5</sub> from the AirKorea network ([airkorea.or.kr](http://airkorea.or.kr)), with the same data selection criteria as for North China.  
 127 The PM<sub>2.5</sub> measurements are made at reference RH ≤ 35%.

128 <sup>c</sup> Major PM<sub>2.5</sub> components including sulfate, nitrate, ammonium, organic carbon, and black carbon at 7 supersites in  
 129 South Korea during KORUS-AQ (May-June 2016; Choi et al., 2019). The mass concentration of organic carbon is  
 130 converted to that of organic aerosol with a multiplicative factor of 1.8 based on KORUS-AQ observations (Kim et  
 131 al., 2018).

132 <sup>d</sup> AODs are from the AERONET Version 3 Level 2.0 all-points database ([aeronet.gsfc.nasa.gov](http://aeronet.gsfc.nasa.gov)), except that AODs  
 133 at the XuZhou site in North China are from the Version 3 Level 1.5 database. AOD at 500 nm (AOD<sub>500nm</sub>) is  
 134 converted to 550 nm (AOD<sub>550nm</sub>) using Ångström Exponent at 500 nm (AE<sub>500nm</sub>) following: AOD<sub>550nm</sub> =  
 135 AOD<sub>500nm</sub>  $\left(\frac{550}{500}\right)^{-AE_{500nm}}$ .

136 <sup>e</sup> AERONET AODs in South Korea are from 10 sites for the full year of 2016 and 21 sites during KORUS-AQ.

137 The KORUS-AQ campaign (Table 2) includes 20 flights over the Korean peninsula and the surrounding ocean from  
 138 May 2 to June 10, 2016, with vertical profiling up to 8 km altitude. We use the aircraft observations of remote and in  
 139 situ aerosol extinction (scattering + absorption) coefficients, dry aerosol number size distributions, sub-micron non-  
 140 refractory aerosol composition, bulk aerosol ionic composition, black carbon (BC), and relative humidity (RH).

141 Geostationary satellite AOD at 550 nm are retrieved by the Yonsei Aerosol Retrieval (YAER) algorithm for the  
 142 GOCI (Choi et al., 2016, 2018) and AHI (Lim et al. 2018) instruments, with GOCI covering East China and South  
 143 Korea and AHI covering the broad East Asia region. AOD from GOCI and AHI have a 6 km × 6 km spatial  
 144 resolution and 1-hour (GOCI) to 2.5-minute (AHI) temporal resolution for 8 hours per day (09:30 to 16:30 local  
 145 time). We use the fused AOD product generated from the Yonsei GOCI and AHI AOD retrievals, each using two  
 146 different surface reflectance methods (Lim et al., 2021). Fusion of this four-member ensemble is done by the  
 147 maximum likelihood estimate (MLE) method, with weighting and averaging based on errors determined by  
 148 comparison to AERONET AOD. The fused satellite AOD product is shown by Lim et al. (2021) to have higher  
 149 accuracy than its member products in comparison with AERONET data during the KORUS-AQ campaign. We will  
 150 refer to it as the ‘GEO satellite AOD’ product in what follows.

Deleted: s

Deleted: East

Deleted: data are

Deleted: rom

Deleted: eastern

Deleted: t

Deleted: ly

Deleted: 0

Deleted: 0

160 **Table 2. KORUS-AQ aircraft observations used in this work (May-June 2016).**

Variable	Instrument
Aerosol extinction profile at 532 nm	HSRL <sup>a</sup>
Aerosol scattering coefficient at 550 nm	TSI nephelometers <sup>b</sup>
Aerosol absorption coefficient at 532 nm	PSAPs <sup>c</sup>
Aerosol dry size distribution	TSI LAS <sup>d</sup>
Bulk aerosol ionic composition	SAGA <sup>e</sup>
Sub-micron non-refractory aerosol composition	HR-ToF-AMS <sup>f</sup>
Black carbon concentration	HDSP2 <sup>g</sup>
Relative humidity	DLH <sup>h</sup>

161 <sup>a</sup> NASA Langley airborne High Spectral Resolution Lidar (HSRL) (Hair et al., 2008; Scarino et al., 2014).

162 <sup>b</sup> NASA Langley TSI-3563 nephelometers (Ziemba et al., 2013).

163 <sup>c</sup> Radiance Research 3-wavelength particle soot absorption photometers (PSAPs; Ziemba et al., 2013).

164 <sup>d</sup> In-situ particle size distributions over the 0.1-5.0 μm diameter range from the TSI Laser Aerosol Spectrometer  
 165 (LAS) Model 3340.

166 <sup>e</sup> University of New Hampshire (UNH) Soluble Acidic Gases and Aerosol (SAGA) instrument (Dibb et al., 2003).  
 167 The cutoff aerodynamic diameter of the inlet is around 4 μm, corresponding to a geometric particle diameter of 2.5  
 168 μm (McNaughton et al., 2007; McNaughton et al., 2009).

169 <sup>f</sup> University of Colorado Boulder High-Resolution Time-of-Flight Aerosol Mass Spectrometer (HR-ToF-AMS;  
 170 DeCarlo et al., 2006; Nault et al., 2018; Guo et al., 2020).

171 <sup>g</sup> NOAA Humidified-Dual-Single-Particle Soot Photometer (HDSP2; Lamb et al., 2018).

172 <sup>h</sup> NASA Diode Laser Hygrometer (DLH; Podolske et al., 2003).

173 **2.2 GEOS-Chem simulation**

174 We use GEOS-Chem version 12.7.1 (DOI: 10.5281/zenodo.3676008) in a nested-grid simulation at a horizontal  
 175 resolution of 0.5° × 0.625° over East Asia (100-145 °E, 20-50 °N). GEOS-Chem simulates detailed tropospheric  
 176 oxidant-aerosol chemistry and is driven here by GEOS-FP assimilated meteorological data from the NASA Global  
 177 Modeling and Assimilation Office (GMAO). Boundary layer mixing uses the non-local scheme implemented by Lin  
 178 and McElroy (2010). Dry deposition of gases and particles follows a standard resistance-in-series scheme (Zhang et  
 179 al., 2001; Fairlie et al., 2007; Fisher et al., 2011; Jaeglé et al., 2018). Wet deposition of gases and particles includes  
 180 contributions from rainout, washout, and scavenging in convective updrafts (Liu et al., 2001; Amos et al., 2012; Q.  
 181 Wang et al., 2011; Q. Wang et al., 2014) with recent updates by Luo et al. (2019, 2020). We use pre-archived initial

Deleted: s

Deleted: s

Deleted: Optical

Deleted: n

Deleted: n

187 conditions from Zhai et al. (2021) and run the model from December 1, 2015 to December 31, 2016. The first month  
188 is used for spin-up and the year 2016 is used for analysis.

189 GEOS-Chem has been used extensively to simulate PM<sub>2.5</sub> and its composition in East Asia (Geng et al., 2017; Li et  
190 al., 2016; Choi et al., 2019; Jeong et al., 2008; Park et al., 2021; Zhai et al., 2021). Here we use the bulk  
191 representation of aerosols including sulfate (Park et al., 2004; Alexander et al., 2009), nitrate (Jaeglé et al., 2018),  
192 primary and secondary organics (Pai et al., 2020), BC (Q. Wang et al., 2014), natural dust in four advected size  
193 ranges (Fairlie et al., 2007), anthropogenic fine dust (Philip et al., 2017), and sea salt in two size ranges (Jaeglé et  
194 al., 2011). Heterogeneous sulfate formation on aqueous aerosols is represented by a simplified parameterization  
195 scheme (Y. Wang et al., 2014), where the SO<sub>2</sub> uptake coefficient ( $\gamma$ ) linearly increases from  $1 \times 10^{-5}$  at RH  $\leq$  50% to  
196  $2 \times 10^{-5}$  at RH = 100%. The thermodynamic equilibrium of sulfate-nitrate-ammonium (SNA) aerosols with the gas  
197 phase is computed with ISORROPIA II (Fountoukis and Nenes, 2007; Pye et al., 2009) assuming an aqueous  
198 aerosol. We include reactive uptake on dust of acid gases (HNO<sub>3</sub>, SO<sub>2</sub>, and H<sub>2</sub>SO<sub>4</sub>), limited by consumption of dust  
199 alkalinity (Fairlie et al., 2010). The alkalinity of emitted dust is estimated by assuming 7.1% Ca<sup>2+</sup> and 1.1% Mg<sup>2+</sup> as  
200 alkaline cations by dust mass (Shah et al., 2020).

201 Monthly anthropogenic emissions are from the Multi-resolution Emission Inventory in 2016 for China (MEIC;  
202 Zheng et al., 2018; <http://meicmodel.org>) and from the KORUSv5 emission inventory at base year 2015 (Woo et al.,  
203 2020; [http://aisl.konkuk.ac.kr/#/emission\\_data/korus-aq\\_emissions](http://aisl.konkuk.ac.kr/#/emission_data/korus-aq_emissions)) for other Asian countries and shipping  
204 emissions. MEIC over China applies weekly and diurnal scaling factors for all anthropogenic emissions (Zheng et  
205 al., 2018). The KORUSv5 agricultural NH<sub>3</sub> emissions apply the diurnal scaling factors from MEIC. Natural  
206 emissions include NO<sub>x</sub> from lightning (Murray et al., 2012) and soil (Hudman et al., 2012), MEGANv2 biogenic  
207 volatile organic compounds (VOCs) (Guenther et al., 2012), dust (Meng et al., 2020), and sea salt (Jaeglé et al.,  
208 2011). Open fire emissions are from the Global Fire Emissions Database version 4 (GFED4; van der Werf et al.,  
209 2017).

### 210 2.3 AOD simulation

211 AOD in GEOS-Chem is diagnosed by integrating vertically the aerosol scattering and absorption coefficients  
212 obtained with a standard Mie calculation applied to assumed size distributions, hygroscopicity, refractive indices,  
213 and densities for individual aerosol components, and summing over all components (Martin et al., 2003). Optical  
214 properties are listed in Table 3. Sulfate, nitrate, and ammonium share the same optical properties and are lumped as  
215 an SNA aerosol component for the purpose of optical calculations. All aerosol components except dust are assumed  
216 to follow log-normal size distributions. Dust includes 7 size bins (centered at radii of 0.15, 0.25, 0.4, 0.8, 1.5, 2.5,  
217 and 4.0  $\mu$ m) for optical calculations, with the smallest four bins partitioned by mass from the first advected dust bin  
218 ( $<$  2.5  $\mu$ m in geometric diameter) following L. Zhang et al. (2013). Dust particles follow a gamma size distribution  
219 within their optical size bins (Curci, 2012). The BC absorption enhancement from coating is as given by X. Wang et  
220 al. (2014).

Deleted: Rokjin

222 Our initial simulations indicated that aerosol extinction coefficients from the standard GEOS-Chem version 12.7.1  
 223 underestimated in situ measured extinction coefficients during KORUS-AQ by 20% on average (Figure S1). We  
 224 traced this problem to bias in the assumed size distributions for SNA and organic aerosol, as shown in Section 3.  
 225 Therefore, we re-computed the diagnostic AOD using updated log-normal size distributions for SNA and organic  
 226 aerosol with number median radius  $R_{N,med} = 0.11 \mu\text{m}$  and geometric standard deviation  $\sigma = 1.4$  based on KORUS-  
 227 AQ observations, instead of  $R_{N,med} = 0.058 \mu\text{m}$  and  $\sigma = 1.6$  in the standard model version 12.7.1, which is derived  
 228 from IMPROVE network measurements of aerosol mass scattering efficiency over North America (Latimer and  
 229 Martin, 2019).

Deleted: (and in Supplementary text and Figure S1-S3)

Deleted: as compared t

230 **Table 3. Aerosol optical properties <sup>a</sup>.**

Aerosol component	$R_{N,med}$ , $\mu\text{m}$	$\sigma$	Hygroscopicity <sup>b</sup>	Refractive index	$\rho$ , $\text{g cm}^{-3}$
SNA <sup>c</sup>	0.11	1.4	$\kappa = 0.61$	$1.53 - 6.0 \times 10^{-3}i$	1.7
Organic <sup>c</sup>	0.11	1.4	$\kappa = 0.1$	$1.53 - 6.0 \times 10^{-3}i$	1.3
BC	0.020	1.6	GADS	$1.75 - 4.4 \times 10^{-3}i$	1.8
Sea salt (fine)	0.085	1.5	GADS	$1.5 - 1.0 \times 10^{-3}i$	2.2
Sea salt (coarse)	0.40	1.8	GADS	$1.5 - 1.0 \times 10^{-3}i$	2.2
Dust	7 size bins	NA	$\kappa = 0^d$	$1.558 - 1.4 \times 10^{-3}i$	2.5-2.65 <sup>e</sup>

231 <sup>a</sup> Aerosol optical properties used in this work for computing aerosol scattering and absorption coefficients. Values  
 232 are from the standard GEOS-Chem model version 12.7.1, except for the size distributions of SNA and organic  
 233 aerosol which are based on KORUS-AQ observations (see text). All aerosol components except dust have log-  
 234 normal dry size distributions where  $R_{N,med}$  is the number median radius and  $\sigma$  is the geometric standard deviation.  
 235 Refractive indices are for 550 nm wavelength.  $\rho$  is the dry aerosol mass density.

236 <sup>b</sup> Hygroscopic growth for SNA and organic aerosol as a function of relative humidity (RH, %) is computed from  $\kappa$ -  
 237 Kohler theory as a diameter growth factor  $GF = (1 + \kappa * RH/(100-RH))^{1/3}$  (Latimer and Martin, 2019). Hygroscopic  
 238 growth factors for other aerosol components are from the Global Aerosol Data Set (GADS) as tabulated in Chin et  
 239 al. (2002) and Martin et al. (2003).

240 <sup>c</sup>  $R_{N,med}$  and  $\sigma$  are fit to KORUS-AQ observations as described in the text. Standard GEOS-Chem v12.7.1 assumes  
 241  $R_{N,med} = 0.058 \mu\text{m}$ ,  $\sigma = 1.6$  (Latimer and Martin, 2019).

242 <sup>d</sup> Hygroscopic growth of dust particles is assumed negligible.

243 <sup>e</sup> Sub-micron dust particles have a density of  $2.5 \text{ g cm}^{-3}$  while coarse mode dust particles have a density of  $2.65 \text{ g}$   
 244  $\text{cm}^{-3}$ . Dust size distribution is described in the text.

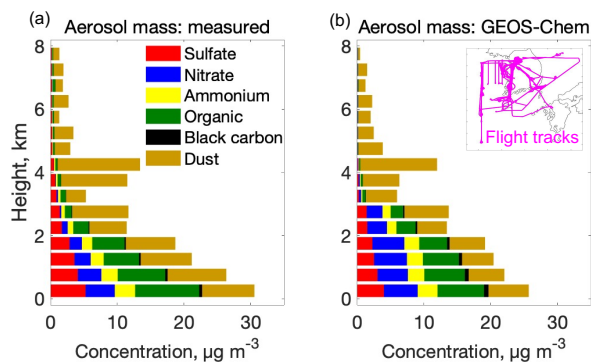
### 245 3 Aerosol concentrations and optical properties during KORUS-AQ

246 Here we use the KORUS-AQ aircraft observations and their simulation with GEOS-Chem to better understand the  
 247 vertical distributions of different aerosol components contributing to AOD over South Korea. We begin with the  
 248 mean vertical profile of aerosol mass and go on to examine the aerosol optical properties. This provides the basis for  
 249 analyzing the observed vertical profile of aerosol extinction, its simulation by GEOS-Chem, and the consistency  
 250 with GEO satellite and AERONET AOD measurements over South Korea during the KORUS-AQ period.

253 **3.1 Vertical profile of aerosol mass**

254 Figure 1 shows the mean vertical profiles of aerosol mass observed during KORUS-AQ and their simulation by  
 255 GEOS-Chem. Here and elsewhere, the model is sampled along the flight tracks and at the flight times. The observed  
 256 vertical distribution of aerosol mass concentrations (Figure 1a) shows that 58% of column aerosol mass is below 2  
 257 km altitude, which we define as the average planetary boundary layer (PBL) during KORUS-AQ, and 34% is at 2-5  
 258 km altitude, which we define as the lower free troposphere (FT). The model has a similar vertical distribution  
 259 (Figure 1b), with 57% of aerosol mass in the PBL and 36% in the lower FT. SNA, organic, and dust each contribute  
 260 about a third of aerosol mass in the PBL while dust dominates in the lower FT both in the observations and in the  
 261 model. The enhanced dust in the lower FT is driven by a few dust events, which the model reproduces (Figure S2).  
 262 Black carbon and sea salt (not shown) make only minor contributions to aerosol mass. The model underestimates  
 263 sulfate by 28% in the PBL, which leads to a 20% overestimate of nitrate, with canceling effect on the SNA mass  
 264 simulation.

265 The GEOS-Chem simulation of organic aerosol in this work uses the simple scheme of Pai et al. (2020) and  
 266 underestimates aircraft observations by 16% in the PBL. Over 90% of GEOS-Chem organic aerosol is secondary,  
 267 consistent with observations (Figure S4; Nault et al., 2018; Pai et al., 2020). GEOS-Chem simulation of the  
 268 KORUS-AQ aerosol component profiles for different meteorological regimes is presented in Park et al. (2021).



269

270 **Figure 1. Vertical profiles of aerosol mass during KORUS-AQ.** Panel (a) shows the mean vertical distributions of  
 271 observed mass concentrations of major aerosol components at ambient temperature and pressure. Panel (b) is the same as  
 272 (a) but from the GEOS-Chem model sampled along the flight tracks (inset). We derive dust concentration from SAGA  
 273  $\text{Ca}^{2+}$  and  $\text{Na}^+$  following Shah et al. (2020) by assuming that non-sea salt  $\text{Ca}^{2+}$  accounts for 7.1% of dust mass:  $[\text{dust}] =$   
 274  $([\text{Ca}^{2+}] - 0.0439 [\text{Na}^+]/2) / 0.071$  where the brackets denote mass concentration. Modeled dust is shown for particles with  
 275 geometric diameter  $< 2.5 \mu\text{m}$ , to be consistent with SAGA measurements (Table 2 footnote e). Measured sulfate, nitrate,  
 276 ammonium, and organic aerosol concentrations are from the AMS instrument (values from the SAGA instrument are  
 277 shown in Figure S4). All data are averaged over 500-m vertical bins. Here and elsewhere, we excluded pollution plumes  
 278 diagnosed by either  $\text{NO}_2$  or  $\text{SO}_2 > 10$  ppbv (3.4% of all the data).

Deleted:



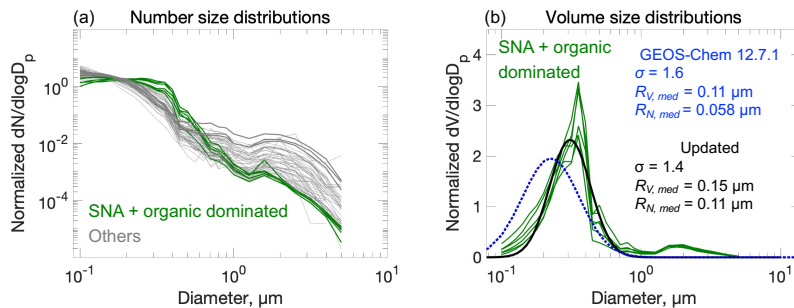
280 **3.2 Aerosol size distributions**

281 Figure 2a shows the normalized dry aerosol number size distributions on each of the 20 flights and in 3 altitude  
 282 bands: < 1.5 km, 3-5 km, and 6-7 km (60 lines). The spread in the size distributions above 1  $\mu\text{m}$  in diameter reflects  
 283 dust influence. We select measurements below 1.5 km altitude when SNA + organic aerosol mass concentrations are  
 284 more than 4 times that of dust as defining the SNA + organic aerosol size distributions (green lines in Figure 2a).  
 285 Conditions dominated by SNA + organic aerosols define the lower envelopes of the ensemble of size distributions at  
 286 diameter > 1  $\mu\text{m}$ . SNA and organics were observed to have similar size distributions during KORUS-AQ (Kim et  
 287 al., 2018).

288 Figure 2b converts the SNA + organic dominated number size distributions to volume size distributions. The  
 289 observed SNA + organic dominated aerosol size distribution is shifted toward larger sizes relative to the standard  
 290 GEOS-Chem. The secondary maximum in the coarse mode could be due to dust. We fitted the observed SNA +  
 291 organic aerosol size distributions to a lognormal distribution with volume median radius  $R_{V,med} = 0.15 \mu\text{m}$  and  
 292 geometric standard deviation  $\sigma = 1.4$ . The number median radius is derived from the volume median radius  
 293 following Seinfeld and Pandis (2016):

$$294 \quad \ln R_{N,med} = \ln R_{V,med} - 3\ln^2\sigma \quad (1)$$

295 which yields  $R_{N,med} = 0.11 \mu\text{m}$ . In comparison, the standard GEOS-Chem size distribution from Latimer and Martin  
 296 (2019) has  $R_{N,med} = 0.058 \mu\text{m}$  and  $\sigma = 1.6$ . We adopt the observed log-normal size distribution parameters in what  
 297 follows (Table 3).



298  
 299 **Figure 2. Aerosol dry size distributions measured in the KORUS-AQ aircraft campaign. Panel (a) shows mean**  
 300 **normalized number size distributions measured on each of the 20 flights and for 3 altitude bins: < 1.5 km, 3-5 km, and 6-7**  
 301 **km (60 lines total). The SNA + organic dominated size distribution profiles are highlighted in color. Panel (b) shows**  
 302 **normalized volume size distributions for conditions dominated by SNA + organic aerosols (green lines), along with a least-**  
 303 **square fit to a lognormal distribution (black line), and the standard GEOS-Chem v12.7.1 size distribution from Latimer**  
 304 **and Martin (2019) (blue dashed line). Normalization imposes an arbitrary value of unit area below each line. Lognormal**

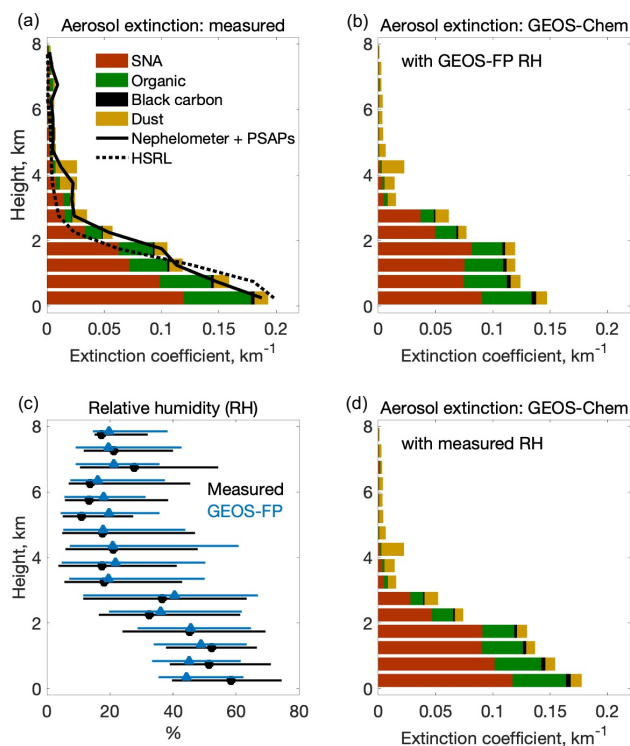
305 distribution parameters are inset in panel (b) including volume median radius ( $R_{V,med}$ ), number median radius ( $R_{N,med}$ ),  
306 and geometric standard deviation ( $\sigma$ ).

### 307 3.3 Aerosol extinction and relation to AOD

308 Figure 3 shows the vertical profiles of ambient aerosol extinction coefficients and RH during KORUS-AQ. Vertical  
309 profiles of aerosol extinction were measured on the aircraft both remotely with the HSRL instrument (above and  
310 below the aircraft) and in situ with TSI-3563 nephelometers (for scattering) and PSAPs (for absorption). The two  
311 agree well, as shown in Figure 3a. They indicate that 76-90% of column aerosol extinction is in the PBL at 0-2 km  
312 altitude and 9-19% is in the lower FT at 2-5 km. Both measurements show that aerosol extinction is much more  
313 strongly weighted to the PBL than aerosol mass (Figure 1).

314 Also shown in Figure 3a are the contributions of individual aerosol components to the extinction profile, as  
315 computed from the GEOS-Chem optical properties (Table 3) applied to the observed mass concentrations. The sum  
316 shows a good match to the measured extinction coefficient profiles. The much larger contribution of the PBL to  
317 column aerosol extinction than to column mass is because aerosol mass in the lower FT is mainly composed of dust,  
318 whose mass extinction efficiency is much smaller than SNA and organics due to its coarse size and lack of  
319 hygroscopic growth (Figure S5). The mean AOD inferred from the aircraft data is 0.36 and is contributed 59% by  
320 SNA, 27% by organic aerosol, 12% by dust, and 2% by BC. It is consistent with the mean AODs measured at  
321 AERONET stations in South Korea during KORUS-AQ (Figure S6).

322 Figure 3b shows the GEOS-Chem simulation of aerosol extinction profiles for comparison to the observations in  
323 Figure 3a. The model underestimates extinction coefficients by 20% below 1 km altitude, [leading to a 10%](#)  
324 [underestimate of aircraft inferred AOD](#), although there is no such underestimate in aerosol mass. This is caused by a  
325 negative RH bias in the GEOS-FP meteorological data used to drive GEOS-Chem, particularly at high RH  
326 conditions (Figure 3c) and is corrected if we apply the observed RH rather than the GEOS-FP RH to the GEOS-  
327 Chem aerosol mass concentrations (Figure 3d).



328  
 329 **Figure 3.** Vertical profiles of aerosol extinction coefficients and relative humidity (RH) during KORUS-AQ. Panel (a)  
 330 shows the mean observed vertical distributions of 550 nm extinction coefficients measured in situ (nephelometer + PSAPs;  
 331 at ambient RH) and remotely (HSRL), along with an independent calculation (colored horizontal bars) from the  
 332 measured mass concentrations of major aerosol components, measured RH, and GEOS-Chem optical properties as given  
 333 in Table 3. Panel (b) shows the mean aerosol extinction profile in GEOS-Chem and the contributions from the different  
 334 model components. Panel (c) is the median vertical profile of RH (horizontal bars are 25-75<sup>th</sup> percentiles) from aircraft  
 335 measurements and the GEOS-FP assimilated meteorological data used to drive GEOS-Chem. Panel (d) is the same as (b)  
 336 but calculated using measured RH.

337 **4 AOD and surface particulate matter over South Korea during KORUS-AQ**

338 Our analysis of Section 3 used the KORUS-AQ aircraft data together with GEOS-Chem to attribute AOD over  
 339 South Korea to individual aerosol components and altitudes. We now take the next step of evaluating the capability  
 340 of GEOS-Chem to independently simulate observed AODs and surface particulate matter concentrations.

**Deleted:** relating satellite to AERONET AODs over the Korea peninsula during KORUS-AQ and

343 Figure 4a shows the spatial distribution of the fused geostationary satellite (GOCI/AHI) AOD (GEO satellite AOD)  
344 during the KORUS-AQ period with AERONET total AOD added as circles. The GEO satellite AOD shows high  
345 values (0.5-0.6) along the west coast of South Korea, significantly correlated with AERONET total AOD with a  
346 spatial correlation coefficient ( $R$ ) of 0.7. GEO satellite AOD is biased low at sites in the Seoul Metropolitan Area  
347 (SMA) and is biased high on the Yellow Sea islands, resulting in an overall -10% bias. The low biases in the SMA  
348 could be due to high-concentration aerosol pixels mis-identified as clouds and/or possible issues with the aerosol  
349 type assumption in the aerosol retrieval, while the high biases on the Yellow Sea islands could result from  
350 uncertainties in the assumption of ocean surface reflectance, as has been discussed by Choi et al. (2016, 2018) and  
351 Lim et al. (2018, 2021). Sampling the AODs at or near the seven PM<sub>2.5</sub> supersites operating during KORUS-AQ  
352 shows no significant bias (inset values in Figure 4a).

Deleted: r

Deleted: , consistent with the validation by Lim et al. (2020)

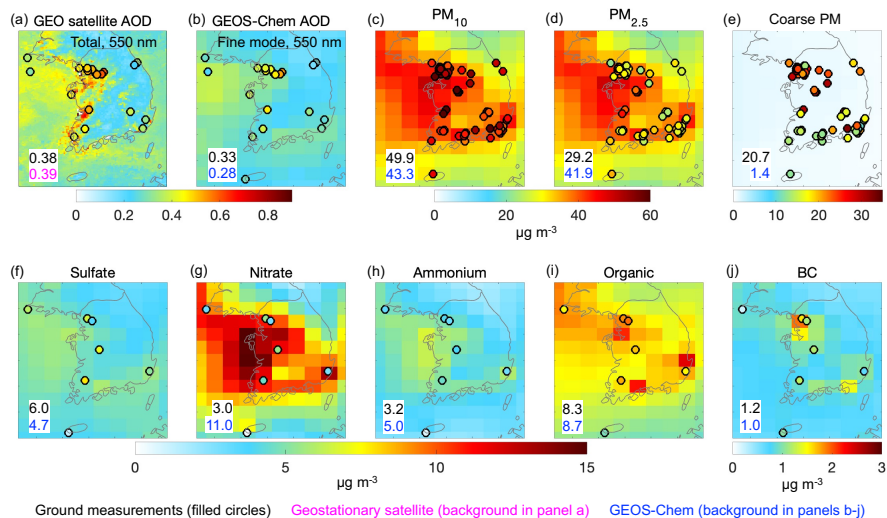
Deleted: are

353 Figure 4b-e shows the spatial distributions of GEOS-Chem AOD, surface PM<sub>10</sub> (particulate matter with aerodynamic  
354 diameter less than 10  $\mu\text{m}$ ), surface PM<sub>2.5</sub>, and surface coarse PM (PM<sub>10</sub> minus PM<sub>2.5</sub>; particulate matter with  
355 aerodynamic diameter less than 10  $\mu\text{m}$  and larger than 2.5  $\mu\text{m}$ ), with surface observations shown as circles and  
356 median values at the measurement sites inset. GEOS-Chem reproduces the satellite AOD enhancements along the  
357 west coast of South Korea but the values are lower than observed, which we attribute to unaccounted coarse PM and  
358 negative RH bias as discussed below. Comparison of AERONET total and fine mode AOD shows a 13%  
359 contribution of coarse particles to total AOD. Comparison of GEOS-Chem to the fine-mode AERONET AOD, as  
360 shown in Figure 4b, finds a 15% underestimate that could be attributed to the low-RH bias (Figure 3c). Concurrent  
361 measurements of PM<sub>10</sub> and PM<sub>2.5</sub> at AirKorea sites show that coarse PM (median 21  $\mu\text{g m}^{-3}$ ) accounts for 41% of  
362 total PM<sub>10</sub> (50  $\mu\text{g m}^{-3}$ ), while coarse PM in GEOS-Chem is much lower (1.4  $\mu\text{g m}^{-3}$ ; Figure 4e). Therefore, about  
363 half of the GEOS-Chem underestimate of total AOD can be attributed to missing coarse PM, with the other half  
364 comes from negative RH bias. Coarse PM has a concentration larger than 10  $\mu\text{g m}^{-3}$  across South Korea, with higher  
365 concentration in the SMA (~ 30  $\mu\text{g m}^{-3}$ ) than in rural areas (~ 15  $\mu\text{g m}^{-3}$ ), implying an origin from both  
366 anthropogenic and natural sources (Figure 4e).

Deleted: mostly

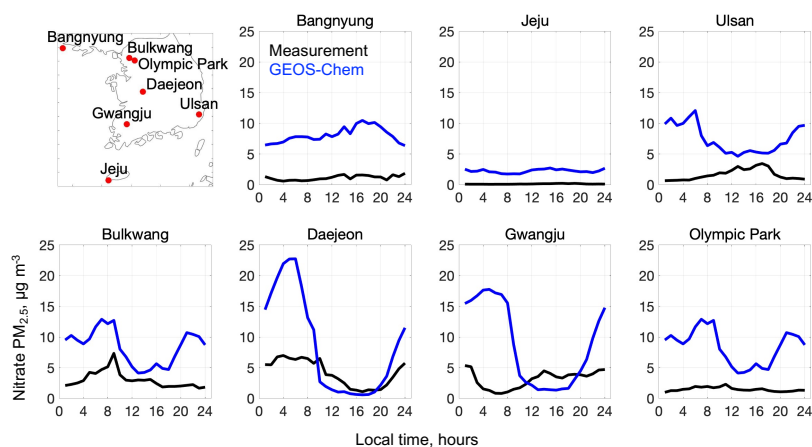
367 GEOS-Chem overestimates surface PM<sub>2.5</sub> by 43% over South Korea (Figure 4d), in contrast to the simulation of  
368 AERONET fine mode AOD (Figure 4b). Figure 4f-j shows the spatial distributions of major PM<sub>2.5</sub> components in  
369 GEOS-Chem (background) and measurements (filled circles). GEOS-Chem is not significantly biased relative to the  
370 observations for organic aerosol and BC, and underestimates sulfate by 22%. We find that the model bias for PM<sub>2.5</sub>  
371 is largely driven by nitrate, which is overestimated by a factor of 3 and leads to a 56% overestimate of ammonium.  
372 By contrast, comparison to the KORUS-AQ data below 1-km altitude showed only a 20% overestimate of nitrate  
373 (Figure 1). This is because the model bias is mainly driven by nighttime conditions, as shown in Figure 5. The cause  
374 of this large model bias is analyzed by K. R. Travis et al. (manuscript in preparation) and is attributed to nighttime  
375 nitrate chemistry and deposition in the stratified boundary layer.

Deleted: n



381  
 382 **Figure 4. Spatial distributions of AOD and surface PM<sub>10</sub>, PM<sub>2.5</sub>, coarse PM (PM<sub>10</sub> minus PM<sub>2.5</sub>), and major PM<sub>2.5</sub>**  
 383 **components over South Korea averaged during KORUS-AQ (May 9 - June 10, 2016). Panel (a) shows the fused**  
 384 **geostationary (GEO) 550 nm AOD from the GOCI and AHI satellites (background) and AERONET 550 nm total AOD**  
 385 **(filled circles). Panel (b) shows GEOS-Chem 550 nm AOD sampled at hourly GEO satellite AOD (GEOS-Chem clear-sky**  
 386 **AOD; background) and AERONET 550 nm fine mode AOD (filled circles). Panel (c) shows surface PM<sub>10</sub> modelled by**  
 387 **GEOS-Chem (background) and measured at ground sites (filled circles). Panels (d-j) are the same as panel (c) but**  
 388 **respectively for PM<sub>2.5</sub>, coarse PM (PM<sub>10</sub> minus PM<sub>2.5</sub>), and sulfate, nitrate, ammonium, organic, and BC PM<sub>2.5</sub>**  
 389 **components. Values inset are median values from ground-based measurements (black) and sampled from GEO satellite**  
 390 **(magenta) and GEOS-Chem (blue). Measured PM<sub>10</sub>, PM<sub>2.5</sub>, and coarse PM in panels (c-e) are shown for a random**  
 391 **selection of 50% of AirKorea sites to visualize spatial distribution, and inset values are for the seven supersites where**  
 392 **PM<sub>2.5</sub> composition was measured. Median AOD values inset are sampled at or near the seven supersites to avoid biasing**  
 393 **by the large number of sites in the Seoul Metropolitan Area. Modelled total PM<sub>2.5</sub> concentrations are calculated at 35%**  
 394 **RH (Table 3). Modelled PM<sub>10</sub> is the sum of PM<sub>2.5</sub>, coarse dust, and coarse sea salt.**

Deleted: ,



396  
 397 **Figure 5. Median diurnal variations of PM<sub>2.5</sub> nitrate concentrations at the seven supersites (top left panel) operated in**  
 398 **South Korea during KORUS-AQ (May 9 - June 10, 2016). Values are medians binned by hour. GEOS-Chem model**  
 399 **values are sampled to coincide with the measurements.**

400 **5 AOD and its relationship to PM<sub>2.5</sub> over East Asia**

401 We build on our analysis of the KORUS-AQ period for a broader interpretation of the distribution of AOD over  
 402 Korea and China and its relationship to surface PM<sub>2.5</sub>, acknowledging that the conditions sampled in KORUS-AQ  
 403 may not be representative of other seasons or of China. Figure 6 shows the spatial distributions of 2016 annual and  
 404 seasonal mean geostationary (GEO) satellite AODs, the corresponding GEOS-Chem clear-sky AODs, and GEOS-  
 405 Chem surface PM<sub>2.5</sub>. The Figure gives normalized mean biases (*NMBs*) relative to ground-based measurements from  
 406 AERONET and from the PM<sub>2.5</sub> surface networks (shown as circles).

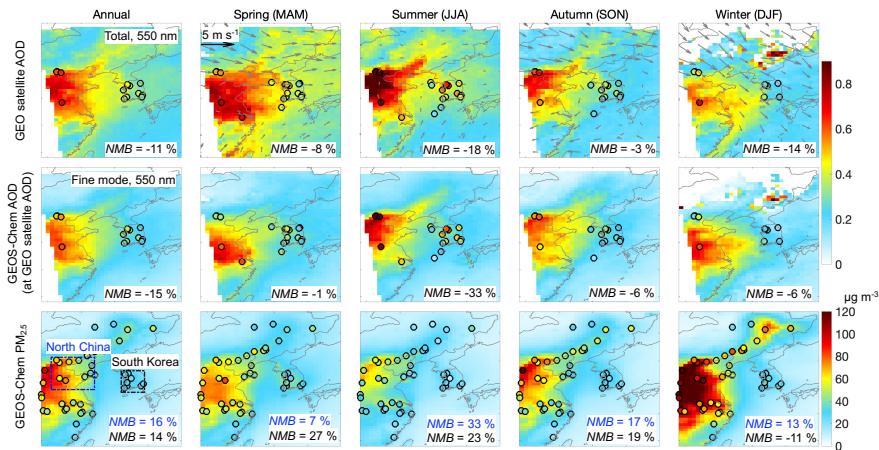
407 On an annual mean basis, AOD over North China (~ 0.5-0.6) is about 50% larger than over South Korea (~ 0.3-0.4).  
 408 AOD over South Korea shows higher values (> 0.4) in the Seoul Metropolitan Area, consistent with that during the  
 409 KORUS-AQ period (Figure 4a). Transport from the Asian continent is strongest in spring when the frequency of  
 410 cold front passages is highest (Liu et al., 2003). AERONET total AOD in spring (0.4-0.6) is twice as large as fine-  
 411 mode AOD (0.2-0.3), reflecting a large contribution of dust. In seasons other than spring, 80-90% of AERONET  
 412 total AOD is contributed by the fine mode. There is large seasonality in AODs over North China, and weaker  
 413 seasonality over South Korea, which will be discussed below.

414 The GEOS-Chem clear-sky AODs show the same spatial and seasonal patterns as GEO satellite AODs but tend to  
 415 be low in spring and summer. Comparison of the model to AERONET AODs confirms this bias and shows better  
 416 agreement with fine-mode AOD in spring (*NMB* of -1%), implying an underestimate of coarse dust that is consistent  
 417 with our comparisons to the AirKorea PM<sub>10</sub> network data (Figure 4e). Comparison of clear-sky and all-sky AODs in

418 GEOS-Chem shows no significant difference on an annual and seasonal mean basis, except for winter (Figure S7).  
 419 Winter has larger all-sky AOD than clear-sky AOD and the lowest rate of successful satellite retrievals (Figure S7),  
 420 which may be due in part to misclassification of heavy wintertime PM<sub>2.5</sub> pollution as clouds (Zhang et al., 2020).

421 The spatial distributions of PM<sub>2.5</sub> in GEOS-Chem in different seasons match closely the observations (Figure 6,  
 422 bottom row). We see also a close coincidence between the spatial distributions of PM<sub>2.5</sub> and AODs, both in the  
 423 observations and the model. On an annual mean basis, GEOS-Chem overestimates PM<sub>2.5</sub> by 16% in North China  
 424 and by 14% in South Korea, even though it underestimates AERONET fine mode AODs by 15%. The overestimate  
 425 of PM<sub>2.5</sub> in South Korea is worst in spring (27%), consistent with KORUS-AQ results which we previously  
 426 attributed to excessive nighttime nitrate build-up in the model. Over North China, the overestimate of PM<sub>2.5</sub> is worst  
 427 in summer (33%), consistent with the nitrate overestimate in summer shown in our previous study (Zhai et al.,  
 428 2021), which could also be due to model overestimate of nighttime nitrate (Miao et al., 2020).

429



430

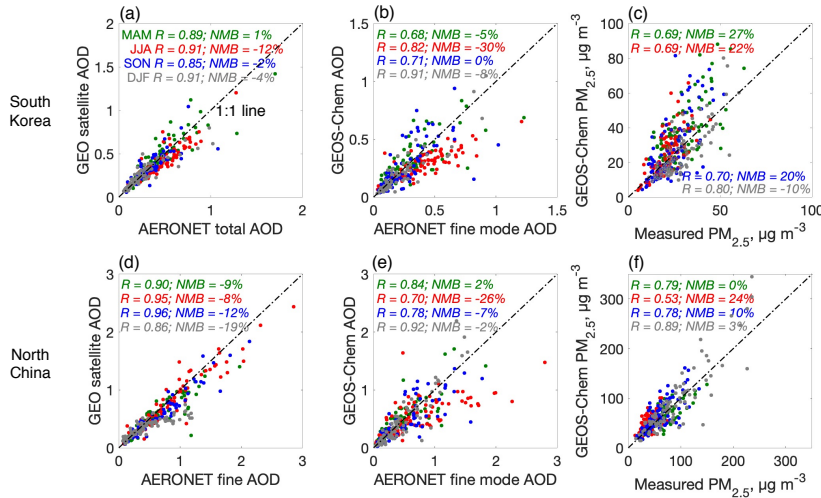
431 **Figure 6. Spatial distributions of 2016 annual and seasonal mean AOD (550 nm) and surface PM<sub>2.5</sub>. The top row shows**  
 432 **the observed GOCI/AHI geostationary satellite AOD (GEO satellite AOD) on the GEOS-Chem 0.5° × 0.625° grid, with**  
 433 **superimposed 925 hPa GEOS-FP wind fields and AERONET total AODs (circles). The middle row shows clear-sky**  
 434 **GEOS-Chem AOD, with AERONET fine mode AOD added as circles. The bottom row shows GEOS-Chem surface PM<sub>2.5</sub>**  
 435 **(background) with surface network measurements (circles). AERONET AODs are shown only when more than 10**  
 436 **months of data are available for the annual mean and all 3 months data are available for each season. The PM<sub>2.5</sub>**  
 437 **observations shown are for a random selection of 7% of network sites for visual clarity. GEOS-Chem PM<sub>2.5</sub> is calculated**

Deleted: s

Deleted: sampled in the same way as hourly GEO satellite AOD (GEOS-Chem clear-sky AOD)

441 at 35% RH (Table 3). Normalized mean biases (NMBs) inset are for the comparisons of GEO satellite and GEOS-Chem  
 442 values to the corresponding ground measurements.

443  
 444 Figure 7 shows daily correlations of the regional average series between AERONET total AOD and GEO satellite  
 445 AOD, between AERONET fine mode AOD and GEOS-Chem AOD, as well as between measured PM<sub>2.5</sub> and GEOS-  
 446 Chem PM<sub>2.5</sub>. Correlations in Figure 7 are all statistically significant with correlation coefficients (*R*) ranging from  
 447 around 0.7 to more than 0.9 and normalized mean biases (NMB) within ± 30%. The correlations of these three pairs  
 448 are similar over South Korea and North China, except that GEOS-Chem overestimates springtime PM<sub>2.5</sub> in South  
 449 Korea but not over North China, possibly due to a model overestimate of the long-range transport of PM<sub>2.5</sub> from  
 450 China to South Korea in spring.



451  
 452 Figure 7. Scatter plots of regional mean daily (a and d) GEO satellite AOD vs. AERONET total AOD, (b and e) GEOS-  
 453 Chem AOD vs. AERONET fine-mode AOD, and (c and f) GEOS-Chem PM<sub>2.5</sub> vs. measured PM<sub>2.5</sub> over South Korea (a-c)  
 454 and North China (d-f). Different colors represent different seasons. Values inset are correlation coefficients (*R*) and  
 455 normalized mean biases (NMB) between surface measurements and GEO satellite or GEOS-Chem values.

457 Figure 8 compares the seasonalities of AOD and PM<sub>2.5</sub> over the North China and South Korea regions. The GEO  
 458 satellite AOD over North China peaks in July and is minimum in winter. Most of AOD is attributed by GEOS-Chem  
 459 to SNA aerosol, same as in South Korea. AOD over South Korea also has a summer maximum and winter minimum  
 460 but with weaker amplitude than over North China. The GEOS-Chem AOD is ~20% biased low in summer and this

Deleted: 7

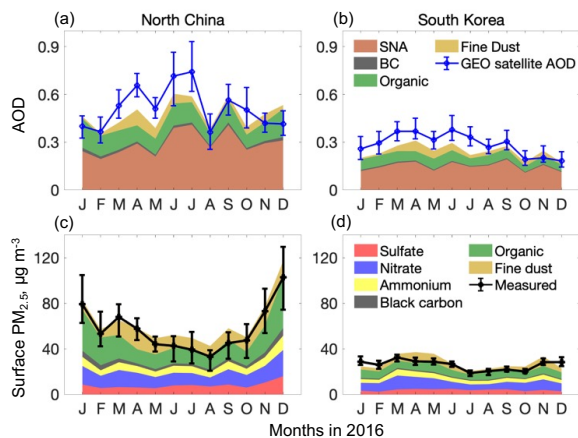
Deleted: model

Deleted: the



464 is largely due to a low RH bias (Figure S8), as seen previously in the KORUS-AQ comparisons but amplified by the  
 465 high RH in summer that drives hygroscopic growth (Latimer and Martin, 2019).

466 Surface PM<sub>2.5</sub> in the observations over North China and South Korea shows opposite seasonality to AOD, with  
 467 minimum values in summer and maximum values in winter-spring. GEOS-Chem reproduces the strong seasonality  
 468 of PM<sub>2.5</sub> in North China and the much weaker seasonality in South Korea. The high PM<sub>2.5</sub> values over North China  
 469 in winter in the model are mostly driven by organic aerosol, reflecting the large residential coal burning source  
 470 (Figure S9; Zheng et al., 2018). In South Korea, by contrast, household energy is mainly from natural gas and  
 471 electricity (Lee et al., 2020; Woo et al., 2020). GEOS-FP daytime PBL height also shows a stronger seasonality over  
 472 North China than over South Korea (Figure S8), generally consistent with the CALIPSO daytime PBL height (Su et  
 473 al., 2018). Previous studies have shown opposite seasonality between MODIS AOD and surface PM<sub>2.5</sub> over North  
 474 China and attributed this to the seasonality in PBL height and RH (Qu et al., 2016; Xu et al., 2019). The mean  
 475 PM<sub>2.5</sub>/AOD ratio over North China in winter (236 μg m<sup>-3</sup>) is 8 times that in summer (29 μg m<sup>-3</sup>), with autumn (94 μg  
 476 m<sup>-3</sup>) and spring (89 μg m<sup>-3</sup>) in between, while over South Korea, the PM<sub>2.5</sub>/AOD ratio in winter (62 μg m<sup>-3</sup>) is only  
 477 70% larger than in summer (36 μg m<sup>-3</sup>).



478  
 479 **Figure 8.** Seasonality of AOD and PM<sub>2.5</sub> over North China and South Korea, and contributions from individual aerosol  
 480 components. Lines show regional medians (error bars: 25<sup>th</sup> and 75<sup>th</sup> percentiles) for the ensemble of monthly averaged  
 481 observations in the regions (Figure 6) in 2016. GEOS-Chem values are shown as stacked contours for individual  
 482 components and are sampled in the same way as the observations.

## 483 6 Conclusions

484 Geostationary satellite observations of aerosol optical depth (AOD) over East Asia may usefully complement PM<sub>2.5</sub>  
 485 air quality networks if the local relationship between AOD and PM<sub>2.5</sub> can be inferred from a physical and/or

Deleted: 7

Deleted: from the GOCI and AHI satellite instruments have tremendous potential for monitoring of

489 statistical model. Here we analyzed the ability of the GEOS-Chem chemical transport model to provide this  
490 relationship by using a new fused GOCI/AHI geostationary satellite product together with AERONET ground-based  
491 AOD measurements, aerosol vertical profiles over South Korea from the KORUS-AQ aircraft campaign (May-June  
492 2016), and surface network observations. This allowed us to identify the critical features and limitations of the  
493 model for successful representing the AOD-PM<sub>2.5</sub> relationship.

494 The KORUS-AQ observations show that total aerosol extinction (550 nm) in the vertical column is dominated by  
495 sulfate-nitrate-ammonium (SNA) and organic aerosol in the planetary boundary layer (PBL), despite large  
496 concentrations of dust in the free troposphere. This reflects the optically effective size and high hygroscopicity of  
497 the PBL aerosols. We find that GEOS-Chem aerosol optical properties based on measurements over North America  
498 (default model setting) underestimate KORUS-AQ aerosol mass extinction efficiency by around 20%. In addition, a  
499 low bias in GEOS-FP RH below 1 km leads to a 10% underestimate of AOD inferred from the aircraft profile.  
500 Adjustments of GEOS-Chem aerosol optical properties and RH enable a successful simulation of the aerosol  
501 extinction profile. SNA aerosol contributes 59% of column aerosol extinction in the KORUS-AQ data, while  
502 organic aerosol contributes 27% and dust contributes 12%.

503 Comparison of GOCI/AHI geostationary (GEO) satellite AOD to AERONET AODs over South Korea shows good  
504 agreement, with high values along the west coast. GEOS-Chem is more consistent with the fine-mode AERONET  
505 AOD because of its insufficient accounting of coarse particles, which account for 13% of AERONET AOD. The  
506 remaining 15% underestimate of AERONET fine-mode AOD by GEOS-Chem can be attributed to the RH low bias.  
507 GEOS-Chem overestimates 24-h surface PM<sub>2.5</sub> over South Korea by 43% during the KORUS-AQ period, despite its  
508 successful simulation of the aircraft data and fine-mode AERONET AOD, and we find that this is due to a large  
509 overestimate of nighttime nitrate.

510 Broader examination of the GOCI/AHI AOD satellite data over East Asia shows spatial distributions and  
511 magnitudes consistent with AERONET and featuring in particular strong Asian outflow in spring that includes a  
512 large dust component. We find that AODs and PM<sub>2.5</sub> have similar large-scale spatial distributions but opposite  
513 seasonality. PM<sub>2.5</sub> in North China has a strong winter maximum and summer minimum, while AOD shows the  
514 opposite. GEOS-Chem simulates successfully the seasonality of measured PM<sub>2.5</sub> but is ~20% biased low in summer  
515 for AOD, due again to RH low bias like that during KORUS-AQ, amplified by the high RH in summer that drives  
516 hygroscopic growth (Latimer and Martin, 2019). We find that the opposite AOD and PM<sub>2.5</sub> seasonality is mainly  
517 driven by residential coal heating sources and low PBL depths in winter, and high RH in summer. Observations of  
518 PM<sub>2.5</sub> and AOD in South Korea show the same seasonal phases as in North China but with much weaker amplitude,  
519 reflecting the lack of residential coal burning in winter and a weaker seasonal amplitude of PBL depth.

520 In summary, we find that the geostationary GOCI/AHI satellite AOD data provide high-quality information for  
521 monitoring of PM<sub>2.5</sub> over East Asia but that physical interpretation requires accurate information on aerosol size  
522 distributions, PBL depths, RH, the role of coarse particles, and diurnal variation of PM<sub>2.5</sub>, all of which are subject to  
523 large uncertainties in chemical transport models. Addressing these uncertainties should be a target of future work.

Deleted: over East Asia if they can be properly interpreted. Here we used

Deleted: PM

Deleted: , simulated collectively with the GEOS-Chem transport model, to better understand the physical relationship between satellite AOD and PM<sub>2.5</sub>

Deleted: 550 nm

Deleted:

Deleted: d

Deleted: , although the simulation is highly sensitive to bias in the relative humidity (RH) of the driving meteorological data

Deleted: the

Deleted: The

Deleted: model

Deleted: d

Deleted: negativ

Deleted: but with

Deleted: amplification

Deleted: is

544 [We have used results from our study in a recent machine-learning reconstruction of daily 2011-present PM<sub>2.5</sub> over](#)  
545 [East Asia from GOCI AOD data by identifying critical variables for the machine-learning algorithm and providing](#)  
546 [blended gap-filling data for cloudy scenes \(Pendergrass et al., 2021\). Besides the factors discussed in this study,](#)  
547 [topography might be another important factor influencing surface PM<sub>2.5</sub> and its vertical mixing \(Su et al., 2018\), and](#)  
548 [this also requires future investigation.](#)

549

550 *Data availability.* Aircraft data during KORUS-AQ are available at: [www-air.larc.nasa.gov/cgi-](http://www-air.larc.nasa.gov/cgi-bin/ArcView/korusaq)  
551 [bin/ArcView/korusaq](http://www-air.larc.nasa.gov/cgi-bin/ArcView/korusaq). PM<sub>2.5</sub> data over China are from: [quotssoft.net/air/](http://quotssoft.net/air/). PM<sub>2.5</sub> data over South Korea are from:  
552 [www.airkorea.or.kr/web](http://www.airkorea.or.kr/web). AERONET data can be found at: [aeronet.gsfc.nasa.gov](http://aeronet.gsfc.nasa.gov). The MEIC emission inventory are  
553 at: [www.meicmodel.org/](http://www.meicmodel.org/). The KORUSv5 emission inventory is developed by Konkuk University, available at:  
554 [http://aisl.konkuk.ac.kr/#/emission\\_data/korus-aq\\_emissions](http://aisl.konkuk.ac.kr/#/emission_data/korus-aq_emissions).

555

556 *Author contributions.* SZ and DJJ designed the study. SZ performed the data analysis and model simulations with  
557 contributions from JFB, KL, HCL, SKK, XW, PL, KRT, and Hong Liao. JK, SL, and Hyunkwang Lim provided  
558 satellite AOD data. RJP and JIJ contributed to AirKorea data processing. JM and RM provided the dust emission  
559 inventory. GL, FY, and JMM updated wet deposition simulation. JWH, BEA, JED, JLJ, PCJ, and BAN contributed  
560 to KORUS-AQ campaign measurements. JHW and YK provided the KORUSv5 emission inventory. QZ provided  
561 the MEIC emission inventory. SZ and DJJ wrote the paper with input from all authors.

562

563 *Acknowledgement.* This work was funded by the Samsung Advanced Institute of Technology and the Harvard-  
564 NUIST Joint Laboratory for Air Quality and Climate (JLAQC). JLJ, PCJ, and BAN acknowledge NASA grant  
565 NNX15AT96G and 80NSSC19K0124 for support.

566

567 *Competing interests.* The authors declare that they have no conflict of interest.

568

## 569 **References**

570 Alexander, B., Park Rokjin, J., Jacob Daniel, J., and Gong, S.: Transition metal-catalyzed oxidation of atmospheric  
571 sulfur: Global implications for the sulfur budget, *J. Geophys. Res. Atmos.*, 114, D02309,  
572 <https://doi.org/10.1029/2008JD010486>, 2009.

573 Amos, H. M., Jacob, D. J., Holmes, C. D., Fisher, J. A., Wang, Q., Yantosca, R. M., Corbitt, E. S., Galarneau, E.,  
574 Rutter, A. P., Gustin, M. S., Steffen, A., Schauer, J. J., Graydon, J. A., Louis, V. L. S., Talbot, R. W., Edgerton, E.  
575 S., Zhang, Y., and Sunderland, E. M.: Gas-particle partitioning of atmospheric Hg(II) and its effect on global  
576 mercury deposition, *Atmos. Chem. Phys.*, 12, 591-603, <https://doi.org/10.5194/acp-12-591-2012>, 2012.

577 Brauer, M., Freedman, G., Frostad, J., van Donkelaar, A., Martin, R. V., Dentener, F., Dingenen, R. v., Estep, K.,  
578 Amini, H., Apte, J. S., Balakrishnan, K., Barregard, L., Broday, D., Feigin, V., Ghosh, S., Hopke, P. K., Knibbs, L.,  
579 D., Kokubo, Y., Liu, Y., Ma, S., Morawska, L., Sangrador, J. L. T., Shaddick, G., Anderson, H. R., Vos, T.,  
580 Forouzanfar, M. H., Burnett, R. T., and Cohen, A.: Ambient Air Pollution Exposure Estimation for the Global  
581 Burden of Disease 2013, *Environ. Sci. Technol.*, 50, 79-88, [10.1021/acs.est.5b03709](https://doi.org/10.1021/acs.est.5b03709), 2016.

582 Brock, C. A., Wagner, N. L., Anderson, B. E., Beyersdorf, A., Campuzano-Jost, P., Day, D. A., Diskin, G. S.,  
583 Gordon, T. D., Jimenez, J. L., Lack, D. A., Liao, J., Markovic, M. Z., Middlebrook, A. M., Perring, A. E.,  
584 Richardson, M. S., Schwarz, J. P., Welti, A., Ziemba, L. D., and Murphy, D. M.: Aerosol optical properties in the  
585 southeastern United States in summer – Part 2: Sensitivity of aerosol optical depth to relative humidity and aerosol  
586 parameters, *Atmos. Chem. Phys.*, 16, 5009-5019, [10.5194/acp-16-5009-2016](https://doi.org/10.5194/acp-16-5009-2016), 2016.

587 Chen, G., Li, S., Knibbs, L. D., Hamm, N. A. S., Cao, W., Li, T., Guo, J., Ren, H., Abramson, M. J., and Guo, Y.: A  
588 machine learning method to estimate PM<sub>2.5</sub> concentrations across China with remote sensing, meteorological and  
589 land use information, *Sci. Total Environ.*, 636, 52-60, <https://doi.org/10.1016/j.scitotenv.2018.04.251>, 2018.

590 Chen, W., Tang, H., and Zhao, H.: Diurnal, weekly and monthly spatial variations of air pollutants and air quality of  
591 Beijing, *Atmos. Environ.*, 119, 21-34, <https://doi.org/10.1016/j.atmosenv.2015.08.040>, 2015.

592 Cheng, Y., Dai, T., Goto, D., Schutgens, N. A. J., Shi, G., and Nakajima, T.: Investigating the assimilation of  
593 CALIPSO global aerosol vertical observations using a four-dimensional ensemble Kalman filter, *Atmos. Chem.*  
594 *Phys.*, 19, 13445-13467, <https://doi.org/10.5194/acp-19-13445-2019>, 2019.

595 Chin, M., Ginoux, P., Kinne, S., Torres, O., Holben, B. N., Duncan, B. N., Martin, R. V., Logan, J. A., Higurashi,  
596 A., and Nakajima, T.: Tropospheric Aerosol Optical Thickness from the GOCART Model and Comparisons with  
597 Satellite and Sun Photometer Measurements, *J. Atmos. Sci.*, 59, 461-483, [https://doi.org/10.1175/1520-0469\(2002\)059<0461:TAOTFT>2.0.CO;2](https://doi.org/10.1175/1520-0469(2002)059<0461:TAOTFT>2.0.CO;2), 2002.

599 Choi, M., Kim, J., Lee, J., Kim, M., Park, Y. J., Holben, B., Eck, T. F., Li, Z., and Song, C. H.: GOCI Yonsei  
600 aerosol retrieval version 2 products: an improved algorithm and error analysis with uncertainty estimation from 5-  
601 year validation over East Asia, *Atmos. Meas. Tech.*, 11, 385-408, [10.5194/amt-11-385-2018](https://doi.org/10.5194/amt-11-385-2018), 2018.

602 Choi, J., Park, R. J., Lee, H.-M., Lee, S., Jo, D. S., Jeong, J. I., Henze, D. K., Woo, J.-H., Ban, S.-J., Lee, M.-D.,  
603 Lim, C.-S., Park, M.-K., Shin, H. J., Cho, S., Peterson, D., and Song, C.-K.: Impacts of local vs. trans-boundary  
604 emissions from different sectors on PM<sub>2.5</sub> exposure in South Korea during the KORUS-AQ campaign, *Atmos.*  
605 *Environ.*, 203, 196-205, <https://doi.org/10.1016/j.atmosenv.2019.02.008>, 2019.

606 Choi, M., Kim, J., Lee, J., Kim, M., Park, Y. J., Jeong, U., Kim, W., Hong, H., Holben, B., Eck, T. F., Song, C. H.,  
607 Lim, J. H., and Song, C. K.: GOCI Yonsei Aerosol Retrieval (YAER) algorithm and validation during the  
608 DRAGON-NE Asia 2012 campaign, *Atmos. Meas. Tech.*, 9, 1377-1398, <https://doi.org/10.5194/amt-9-1377-2016>,  
609 2016.

610 Crawford, J. H., Ahn, J. Y., Al-Saadi, J., Chang, L., Emmons, L., Kim, J., Lee, G., Park, J. H., Park, R., Woo, J. H.,  
611 Song, C. K., Hong, J.-H., Hong, Y.-D., Lefer, B. L., Lee, M., Lee, T., Kim, S., Min, K.-E., Yum, S. S., Shin, H. J.,  
612 Kim, Y.-W., Choi, J.-S., Park, J.-S., Szykman, J. J., Long, R. W., Jordan, C. E., Simpson, I. J., Fried, A., Dibb, J. E.,  
613 Cho, S. Y., and Kim, Y. P.: The Korea-United States air quality (KORUS-AQ) field study, *Elementa-Sci. Anthropol.*,  
614 in press, 2021.

615 Curci, G.: FlexAOD: a chemistry-transport model post-processing tool for a flexible calculation of aerosol optical  
616 properties, 1-4, [http://pumpkin.aquila.infn.it/gabri/download/curci\\_istp2012.pdf](http://pumpkin.aquila.infn.it/gabri/download/curci_istp2012.pdf), 2012.

617 Dai, Q., Bi, X., Liu, B., Li, L., Ding, J., Song, W., Bi, S., Schulze, B. C., Song, C., Wu, J., Zhang, Y., Feng, Y., and  
618 Hopke, P. K.: Chemical nature of PM<sub>2.5</sub> and PM<sub>10</sub> in Xi'an, China: Insights into primary emissions and secondary  
619 particle formation, *Environmental Pollution*, 240, 155-166, <https://doi.org/10.1016/j.envpol.2018.04.111>, 2018.

620 Di, Q., Amini, H., Shi, L., Kloog, I., Silvern, R., Kelly, J., Sabath, M. B., Choirat, C., Koutrakis, P., Lyapustin, A.,  
621 Wang, Y., Mickley, L. J., and Schwartz, J.: An ensemble-based model of PM<sub>2.5</sub> concentration across the contiguous  
622 United States with high spatiotemporal resolution, *Environ. Int.*, 130, 104909,  
623 <https://doi.org/10.1016/j.envint.2019.104909>, 2019.

- 624 Dibb, J. E., Talbot, R. W., Scheuer, E. M., Seid, G., Avery, M. A., and Singh, H. B.: Aerosol chemical composition  
625 in Asian continental outflow during the TRACE-P campaign: Comparison with PEM-West B, *J. Geophys. Res.*  
626 *Atmos.*, 108, 8815, <https://doi.org/10.1029/2002JD003111>, 2003.
- 627 Fairlie, T. D., Jacob, D. J., and Park, R. J.: The impact of transpacific transport of mineral dust in the United States,  
628 *Atmos. Environ.*, 41, 1251-1266, <https://doi.org/10.1016/j.atmosenv.2006.09.048>, 2007.
- 629 Fairlie, T. D., Jacob, D. J., Dibb, J. E., Alexander, B., Avery, M. A., van Donkelaar, A., and Zhang, L.: Impact of  
630 mineral dust on nitrate, sulfate, and ozone in transpacific Asian pollution plumes, *Atmos. Chem. Phys.*, 10, 3999-  
631 4012, <https://doi.org/10.5194/acp-10-3999-2010>, 2010.
- 632 Fisher, J. A., Jacob, D. J., Wang, Q., Bahreini, R., Carouge, C. C., Cubison, M. J., Dibb, J. E., Diehl, T., Jimenez, J.  
633 L., Leibensperger, E. M., Lu, Z., Meinders, M. B. J., Pye, H. O. T., Quinn, P. K., Sharma, S., Streets, D. G., van  
634 Donkelaar, A., and Yantosca, R. M.: Sources, distribution, and acidity of sulfate-ammonium aerosol in the Arctic in  
635 winter-spring, *Atmos. Environ.*, 45, 7301-7318, <https://doi.org/10.1016/j.atmosenv.2011.08.030>, 2011.
- 636 Fountoukis, C. and Nenes, A.: ISORROPIA II: a computationally efficient thermodynamic equilibrium model for  
637  $K^+$ - $Ca^{2+}$ - $Mg^{2+}$ - $NH_4^+$ - $Na^+$ - $SO_4^{2-}$ - $NO_3^-$ - $Cl^-$ - $H_2O$  aerosols, *Atmos. Chem. Phys.*, 7, 4639-4659,  
638 <https://doi.org/10.5194/acp-7-4639-2007>, 2007.
- 639 Geng, G., Zhang, Q., Tong, D., Li, M., Zheng, Y., Wang, S., and He, K.: Chemical composition of ambient  $PM_{2.5}$   
640 over China and relationship to precursor emissions during 2005-2012, *Atmos. Chem. Phys.*, 17, 9187-9203,  
641 <https://doi.org/10.5194/acp-17-9187-2017>.
- 642 Giles, D. M., Sinyuk, A., Sorokin, M. G., Schafer, J. S., Smirnov, A., Slutsker, I., Eck, T. F., Holben, B. N., Lewis,  
643 J. R., Campbell, J. R., Welton, E. J., Korkin, S. V., and Lyapustin, A. I.: Advancements in the Aerosol Robotic  
644 Network (AERONET) Version 3 database - automated near-real-time quality control algorithm with improved cloud  
645 screening for Sun photometer aerosol optical depth (AOD) measurements, *Atmos. Meas. Tech.*, 12, 169-209,  
646 <https://doi.org/10.5194/amt-12-169-2019>, 2019.
- 647 Guenther, A. B., Jiang, X., Heald, C. L., Sakulyanontvittaya, T., Duhl, T., Emmons, L. K., and Wang, X.: The  
648 Model of Emissions of Gases and Aerosols from Nature version 2.1 (MEGAN2.1): an extended and updated  
649 framework for modeling biogenic emissions, *Geosci. Model Dev.*, 5, 1471-1492, <https://doi.org/10.5194/gmd-5-1471-2012>, 2012.
- 651 [Guo, J., Xia, F., Zhang, Y., Liu, H., Li, J., Lou, M., He, J., Yan, Y., Wang, F., Min, M., and Zhai, P.: Impact of](#)  
652 [diurnal variability and meteorological factors on the  \$PM\_{2.5}\$  - AOD relationship: Implications for  \$PM\_{2.5}\$  remote](#)  
653 [sensing, \*Environ. Pollut.\*, 221, 94-104, <https://doi.org/10.1016/j.envpol.2016.11.043>, 2017.](#)
- 654 Guo, H., Campuzano-Jost, P., Nault, B. A., Day, D. A., Schroder, J. C., Dibb, J. E., Dollner, M., Weinzierl, B., and  
655 Jimenez, J. L.: The Importance of Size Ranges in Aerosol Instrument Intercomparisons: A Case Study for the ATom  
656 Mission, *Atmos. Meas. Tech. Discuss.*, 2020, 1-49, <https://doi.org/10.5194/amt-2020-224>, 2020.
- 657 Hair, J. W., Hostetler, C. A., Cook, A. L., Harper, D. B., Ferrare, R. A., Mack, T. L., Welch, W., Izquierdo, L. R.,  
658 and Hovis, F. E.: Airborne High Spectral Resolution Lidar for profiling aerosol optical properties, *Appl. Opt.*, 47,  
659 6734-6752, <https://doi.org/10.1364/AO.47.006734>, 2008.
- 660 Hammer, M. S., van Donkelaar, A., Li, C., Lyapustin, A., Sayer, A. M., Hsu, N. C., Levy, R. C., Garay, M.,  
661 Kalashnikova, O., Kahn, R. A., Brauer, M., Apte, J. S., Henze, D. K., Zhang, L., Zhang, Q., Ford, B., Pierce, J. R.,  
662 and Martin, R. V.: Global Estimates and Long-Term Trends of Fine Particulate Matter Concentrations (1998-2018),  
663 *Environ. Sci. Technol.*, 54, 7879-7890, <https://dx.doi.org/10.1021/acs.est.0c01764>, 2020.
- 664 [Hu, X., Belle, J. H., Meng, X., Wildani, A., Waller, L. A., Strickland, M. J., and Liu, Y.: Estimating  \$PM\_{2.5}\$](#)   
665 [Concentrations in the Conterminous United States Using the Random Forest Approach, \*Environ. Sci. Technol.\*, 51,](#)  
666 [6936-6944, \[10.1021/acs.est.7b01210\]\(https://doi.org/10.1021/acs.est.7b01210\), 2017.](#)
- 667 Hudman, R. C., Moore, N. E., Mebust, A. K., Martin, R. V., Russell, A. R., Valin, L. C., and Cohen, R. C.: Steps  
668 towards a mechanistic model of global soil nitric oxide emissions: implementation and space based-constraints,  
669 *Atmos. Chem. Phys.*, 12, 7779-7795, <https://doi.org/10.5194/acp-12-7779-2012>, 2012.
- 670 Jaeglé, L., Quinn, P. K., Bates, T. S., Alexander, B., and Lin, J. T.: Global distribution of sea salt aerosols: new  
671 constraints from in situ and remote sensing observations, *Atmos. Chem. Phys.*, 11, 3137-3157,  
672 <https://doi.org/10.5194/acp-11-3137-2011>, 2011.

673 Jaeglé, L., Shah, V., Thornton, J. A., Lopez-Hilfiker, F. D., Lee, B. H., McDuffie, E. E., Fibiger, D., Brown, S. S.,  
674 Veres, P., Sparks, T. L., Ebben, C. J., Wooldridge, P. J., Kenagy, H. S., Cohen, R. C., Weinheimer, A. J., Campos,  
675 T. L., Montzka, D. D., Digangi, J. P., Wolfe, G. M., Hanisco, T., Schroder, J. C., Campuzano-Jost, P., Day, D. A.,  
676 Jimenez, J. L., Sullivan, A. P., Guo, H., and Weber, R. J.: Nitrogen Oxides Emissions, Chemistry, Deposition, and  
677 Export Over the Northeast United States During the WINTER Aircraft Campaign, *J. Geophys. Res. Atmos.*, 123,  
678 12,368-312,393, <https://doi.org/10.1029/2018JD029133>, 2018.

679 Jeong, J. I., Park, R. J., and Youn, D.: Effects of Siberian forest fires on air quality in East Asia during May 2003  
680 and its climate implication, *Atmos. Environ.*, 42, 8910-8922, <https://doi.org/10.1016/j.atmosenv.2008.08.037>, 2008.

681 Jordan, C. E., Crawford, J. H., Beyersdorf, A. J., Eck, T. F., Halliday, H. S., Nault, B. A., Chang, L.-S., Park, J.,  
682 Park, R., and Lee, G.: Investigation of factors controlling PM<sub>2.5</sub> variability across the South Korean Peninsula during  
683 KORUS-AQ, *Elementa-Sci. Anthropol.*, 8, 28, <https://doi.org/10.1525/elementa.424>, 2020.

684 Kim, H., Zhang, Q., and Heo, J.: Influence of intense secondary aerosol formation and long-range transport on  
685 aerosol chemistry and properties in the Seoul Metropolitan Area during spring time: results from KORUS-AQ,  
686 *Atmos. Chem. Phys.*, 18, 7149-7168, <https://doi.org/10.5194/acp-18-7149-2018>, 2018.

687 Kumar, R., Delle Monache, L., Bresch, J., Saide, P. E., Tang, Y., Liu, Z., da Silva, A. M., Alessandrini, S., Pfister,  
688 G., Edwards, D., Lee, P., and Djalalova, I.: Toward Improving Short-Term Predictions of Fine Particulate Matter  
689 Over the United States Via Assimilation of Satellite Aerosol Optical Depth Retrievals, *J. Geophys. Res. Atmos.*,  
690 124, 2753-2773, <https://doi.org/10.1029/2018JD029009>, 2019.

691 Lamb, K. D., Perring, A. E., Samset, B., Peterson, D., Davis, S., Anderson, B. E., Beyersdorf, A., Blake, D. R.,  
692 Campuzano-Jost, P., Corr, C. A., Diskin, G. S., Kondo, Y., Moteki, N., Nault, B. A., Oh, J., Park, M., Pusede, S. E.,  
693 Simpson, I. J., Thornhill, K. L., Wisthaler, A., and Schwarz, J. P.: Estimating Source Region Influences on Black  
694 Carbon Abundance, Microphysics, and Radiative Effect Observed Over South Korea, *J. Geophys. Res. Atmos.*, 123,  
695 13,527-513,548, <https://doi.org/10.1029/2018JD029257>, 2018.

696 Latimer, R. N. C. and Martin, R. V.: Interpretation of measured aerosol mass scattering efficiency over North  
697 America using a chemical transport model, *Atmos. Chem. Phys.*, 19, 2635-2653, <https://doi.org/10.5194/acp-19-2635-2019>, 2019.

699 Lee, W., Lim, T., and Kim, D. D.: Thermal and Energy Performance Assessment of the Prefab Electric Ondol  
700 System for Floor Heating in a Residential Building, *Energies*, 13, 5723, <https://doi.org/10.3390/en13215723>, 2020.

701 [Lennartson, E. M., Wang, J., Gu, J., Castro Garcia, L., Ge, C., Gao, M., Choi, M., Saide, P. E., Carmichael, G. R.,](#)  
702 [Kim, J., and Janz, S. J.: Diurnal variation of aerosol optical depth and PM<sub>2.5</sub> in South Korea: a synthesis from](#)  
703 [AERONET, satellite \(GOCI\), KORUS-AQ observation, and the WRF-Chem model, \*Atmos. Chem. Phys.\*, 18,](#)  
704 [15125-15144, 10.5194/acp-18-15125-2018, 2018.](#)

705 Li, K., Liao, H., Zhu, J., and Moch Jonathan, M.: Implications of RCP emissions on future PM<sub>2.5</sub> air quality and  
706 direct radiative forcing over China, *J. Geophys. Res. Atmos.*, 121, 12,985-913,008,  
707 <https://doi.org/10.1002/2016JD025623>, 2016.

708 Lim, H., Choi, M., Kim, J., Kasai, Y., and Chan, P.: AHI/Himawari-8 Yonsei Aerosol Retrieval (YAER):  
709 Algorithm, Validation and Merged Products, *Remote Sens.*, 10, 699, <https://doi.org/10.3390/rs10050699>, 2018.

710 [Lim, H., Go, S., Kim, J., Choi, M., Lee, S., Song, C. K., and Kasai, Y.: Integration of GOCI and AHI Yonsei aerosol](#)  
711 [optical depth products during the 2016 KORUS-AQ and 2018 EMeRGe campaigns, \*Atmos. Meas. Tech.\*, 14, 4575-](#)  
712 [4592, 10.5194/amt-14-4575-2021, 2021.](#)

713 Lin, J. and McElroy, M. B.: Impacts of boundary layer mixing on pollutant vertical profiles in the lower  
714 troposphere: Implications to satellite remote sensing, *Atmos. Environ.*, 44, 1726-1739,  
715 <https://doi.org/10.1016/j.atmosenv.2010.02.009>, 2010.

716 Liu, H., Jacob, D. J., Bey, I., and Yantosca, R. M.: Constraints from <sup>210</sup>Pb and <sup>7</sup>Be on wet deposition and transport in  
717 a global three-dimensional chemical tracer model driven by assimilated meteorological fields, *J. Geophys. Res.*  
718 *Atmos.*, 106, 12109-12128, <https://doi.org/10.1029/2000JD900839>, 2001.

719 Liu, H., Jacob Daniel, J., Bey, I., Yantosca Robert, M., Duncan Bryan, N., and Sachse Glen, W.: Transport pathways  
720 for Asian pollution outflow over the Pacific: Interannual and seasonal variations, *J. Geophys. Res. Atmos.*, 108,  
721 8786, <https://doi.org/10.1029/2002JD003102>, 2003.

**Deleted:** Lee, S., Kim, J., Choi, M., Hong, J., Lim, H., Eck, T. F., Holben, B. N., Ahn, J.-Y., Kim, J., and Koo, J.-H.: Analysis of long-range transboundary transport (LRTT) effect on Korean aerosol pollution during the KORUS-AQ campaign, *Atmos. Environ.*, 204, 53-67, <https://doi.org/10.1016/j.atmosenv.2019.02.020>, 2019.

**Deleted:** Lim, H., Go, S., Kim, J., Choi, M., Lee, S., Song, C. K., and Kasai, Y.: Integration of GOCI and AHI Yonsei Aerosol Optical Depth Products During the 2016 KORUS-AQ and 2018 EMeRGe Campaigns, *Atmos. Meas. Tech. Discuss.*, 2020, 1-32, <https://doi.org/10.5194/amt-2020-336>, 2020.

734 [Liu, P., Zhao, C., Liu, P., Deng, Z., Huang, M., Ma, X., and Tie, X.: Aircraft study of aerosol vertical distributions](#)  
735 [over Beijing and their optical properties, \*Tellus B Chem. Phys. Meteorol.\*, 61, 756-767, 10.1111/j.1600-](#)  
736 [0889.2009.00440.x, 2009.](#)

737 Liu, Y., Park, R. J., Jacob, D. J., Li, Q., Kilaru, V., and Sarnat, J. A.: Mapping annual mean ground-level PM<sub>2.5</sub>  
738 concentrations using Multiangle Imaging Spectroradiometer aerosol optical thickness over the contiguous United  
739 States, *J. Geophys. Res. Atmos.*, 109, D22206, <https://doi.org/10.1029/2004JD005025>, 2004.

740 Luo, G., Yu, F., and Moch, J. M.: Further improvement of wet process treatments in GEOS-Chem v12.6.0: impact  
741 on global distributions of aerosols and aerosol precursors, *Geosci. Model Dev.*, 13, 2879-2903,  
742 <https://doi.org/10.5194/gmd-13-2879-2020>, 2020.

743 Luo, G., Yu, F., and Schwab, J.: Revised treatment of wet scavenging processes dramatically improves GEOS-Chem  
744 12.0.0 simulations of nitric acid, nitrate, and ammonium over the United States, *Geosci. Model Dev.*, 12, 3439-3447  
745 <https://doi.org/10.5194/gmd-12-3439-2019>, 2019.

746 Martin, R. V., Jacob, D. J., Yantosca, R. M., Chin, M., and Ginoux, P.: Global and regional decreases in  
747 tropospheric oxidants from photochemical effects of aerosols, *J. Geophys. Res. Atmos.*, 108, 4097,  
748 <https://doi.org/10.1029/2002JD002622>, 2003.

749 McNaughton, C. S., Clarke, A. D., Howell, S. G., Pinkerton, M., Anderson, B., Thornhill, L., Hudgins, C.,  
750 Winstead, E., Dibb, J. E., Scheuer, E., and Maring, H.: Results from the DC-8 Inlet Characterization Experiment  
751 (DICE): Airborne Versus Surface Sampling of Mineral Dust and Sea Salt Aerosols, *Aerosol Sci. Tech.*, 41, 136-159,  
752 <https://doi.org/10.1080/02786820601118406>, 2007.

753 McNaughton, C. S., Clarke, A. D., Kapustin, V., Shinozuka, Y., Howell, S. G., Anderson, B. E., Winstead, E., Dibb,  
754 J., Scheuer, E., Cohen, R. C., Wooldridge, P., Perring, A., Huey, L. G., Kim, S., Jimenez, J. L., Dunlea, E. J.,  
755 DeCarlo, P. F., Wennberg, P. O., Crouse, J. D., Weinheimer, A. J., and Flocke, F.: Observations of heterogeneous  
756 reactions between Asian pollution and mineral dust over the Eastern North Pacific during INTEX-B, *Atmos. Chem.*  
757 *Phys.*, 9, 8283-8308, <https://doi.org/10.5194/acp-9-8283-2009>, 2009.

758 Meng, J., Martin, R. V., Ginoux, P., Hammer, M., Sulprizio, M. P., Ridley, D. A., and van Donkelaar, A.: Grid-  
759 independent High Resolution Dust Emissions (v1.0) for Chemical Transport Models: Application to GEOS-Chem  
760 (version 12.5.0), *Geosci. Model Dev. Discuss.*, 1-23, <https://doi.org/10.5194/gmd-2020-380>, 2020.

761 Miao, R., Chen, Q., Zheng, Y., Cheng, X., Sun, Y., Palmer, P. I., Shrivastava, M., Guo, J., Zhang, Q., Liu, Y., Tan,  
762 Z., Ma, X., Chen, S., Zeng, L., Lu, K., and Zhang, Y.: Model bias in simulating major chemical components of  
763 PM<sub>2.5</sub> in China, *Atmos. Chem. Phys.*, 20, 12265-12284, <https://doi.org/10.5194/acp-20-12265-2020>, 2020.

764 Murray, L. T., Jacob, D. J., Logan, J. A., Hudman, R. C., and Koshak, W. J.: Optimized regional and interannual  
765 variability of lightning in a global chemical transport model constrained by LIS/OTD satellite data, *J. Geophys. Res.*  
766 *Atmos.*, 117, D20307, <https://doi.org/10.1029/2012JD017934>, 2012.

767 Nault, B. A., Campuzano-Jost, P., Day, D. A., Schroder, J. C., Anderson, B., Beyersdorf, A. J., Blake, D. R., Brune,  
768 W. H., Choi, Y., Corr, C. A., de Gouw, J. A., Dibb, J., DiGangi, J. P., Diskin, G. S., Fried, A., Huey, L. G., Kim, M.  
769 J., Knote, C. J., Lamb, K. D., Lee, T., Park, T., Pusede, S. E., Scheuer, E., Thornhill, K. L., Woo, J. H., and Jimenez,  
770 J. L.: Secondary organic aerosol production from local emissions dominates the organic aerosol budget over Seoul,  
771 South Korea, during KORUS-AQ, *Atmos. Chem. Phys.*, 18, 17769-17800, [https://doi.org/10.5194/acp-18-17769-](https://doi.org/10.5194/acp-18-17769-2018)  
772 [2018](#), 2018.

773 [O'Neill, N. T., Eck, T. F., Smirnov, A., Holben, B. N., and Thulasiraman, S.: Spectral discrimination of coarse and](#)  
774 [fine mode optical depth, \*J. Geophys. Res. Atmos.\*, 108, https://doi.org/10.1029/2002JD002975, 2003.](#)

775 Pai, S. J., Heald, C. L., Pierce, J. R., Farina, S. C., Marais, E. A., Jimenez, J. L., Campuzano-Jost, P., Nault, B. A.,  
776 Middlebrook, A. M., Coe, H., Shilling, J. E., Bahreini, R., Dingle, J. H., and Vu, K.: An evaluation of global organic  
777 aerosol schemes using airborne observations, *Atmos. Chem. Phys.*, 20, 2637-2665, [https://doi.org/10.5194/acp-20-](https://doi.org/10.5194/acp-20-2637-2020)  
778 [2637-2020](#), 2020.

779 Park, R. J., Oak, Y. J., Emmons, L. K., Kim, C.-H., Pfister, G. G., Carmichael, G. R., Saide, P. E., Cho, S.-Y., Kim,  
780 S., Woo, J.-H., Crawford, J. H., Gaubert, B., Lee, H.-J., Park, S.-Y., Jo, Y.-J., Gao, M., Tang, B., Stanier, C. O.,  
781 Shin, S. S., Park, H. Y., Bae, C., and Kim, E.: Multi-model intercomparisons of air quality simulations for the  
782 KORUS-AQ campaign, *Elementa-Sci. Anthropol.*, 9, 00139, <https://doi.org/10.1525/elementa.2021.00139>, 2021.



783 Park Rokjin, J., Jacob Daniel, J., Field Brendan, D., Yantosca Robert, M., and Chin, M.: Natural and transboundary  
784 pollution influences on sulfate-nitrate-ammonium aerosols in the United States: Implications for policy, *J. Geophys.*  
785 *Res. Atmos.*, 109, D15204, <https://doi.org/10.1029/2003JD004473>, 2004.

786 [Pendergrass, D. C., Jacob, D. J., Zhai, S., Kim, J., Koo, J. H., Lee, S., Bae, M., Kim, S.: Continuous mapping of fine  
787 particulate matter \(PM<sub>2.5</sub>\) air quality in East Asia at daily 6x6 km<sup>2</sup> resolution by application of a random forest  
788 algorithm to 2011-2019 GOCI geostationary satellite data, submitted, 2021.](#)

789 Peterson, D. A., Hyer, E. J., Han, S.-O., Crawford, J. H., Park, R. J., Holz, R., Kuehn, R. E., Eloranta, E., Knote, C.,  
790 Jordan, C. E., and Lefer, B. L.: Meteorology influencing springtime air quality, pollution transport, and visibility in  
791 Korea, *Elementa-Sci. Anthropol.*, 7, 57, <https://doi.org/10.1525/elementa.395>, 2019.

792 Philip, S., Martin, R. V., Snider, G., Weagle, C. L., van Donkelaar, A., Brauer, M., Henze, D. K., Klimont, Z.,  
793 Venkataraman, C., and Guttikunda, S. K.: Anthropogenic fugitive, combustion and industrial dust is a significant,  
794 underrepresented fine particulate matter source in global atmospheric models, *Environ. Res. Lett.*, 12, 044018,  
795 <https://doi.org/10.1088/1748-9326/aa65a4>, 2017.

796 Podolske, J. R., Sachse, G. W., and Diskin, G. S.: Calibration and data retrieval algorithms for the NASA  
797 Langley/Ames Diode Laser Hygrometer for the NASA Transport and Chemical Evolution Over the Pacific  
798 (TRACE-P) mission, *J. Geophys. Res. Atmos.*, 108, 8792, <https://doi.org/10.1029/2002JD003156>, 2003.

799 Pye, H. O. T., Liao, H., Wu, S., Mickley, L. J., Jacob, D. J., Henze, D. K., and Seinfeld, J. H.: Effect of changes in  
800 climate and emissions on future sulfate-nitrate-ammonium aerosol levels in the United States, *J. Geophys. Res.*  
801 *Atmos.*, 114, D01205, <https://doi.org/10.1029/2008JD010701>, 2009.

802 [Qu, W., Wang, J., Zhang, X., Sheng, L., and Wang, W.: Opposite seasonality of the aerosol optical depth and the  
803 surface particulate matter concentration over the north China Plain, \*Atmos. Environ.\*, 127, 90-99,  
804 <https://doi.org/10.1016/j.atmosenv.2015.11.061>, 2016.](#)

805 Saide, P. E., Kim, J., Song, C. H., Choi, M., Cheng, Y., and Carmichael, G. R.: Assimilation of next generation  
806 geostationary aerosol optical depth retrievals to improve air quality simulations, *Geophys. Res. Lett.*, 41, 9188-9196,  
807 <https://doi.org/10.1002/2014GL062089>, 2014.

808 Saide, P. E., Gao, M., Lu, Z., Goldberg, D. L., Streets, D. G., Woo, J. H., Beyersdorf, A., Corr, C. A., Thornhill, K.  
809 L., Anderson, B., Hair, J. W., Nehrir, A. R., Diskin, G. S., Jimenez, J. L., Nault, B. A., Campuzano-Jost, P., Dibb, J.,  
810 Heim, E., Lamb, K. D., Schwarz, J. P., Perring, A. E., Kim, J., Choi, M., Holben, B., Pfister, G., Hodzic, A.,  
811 Carmichael, G. R., Emmons, L., and Crawford, J. H.: Understanding and improving model representation of aerosol  
812 optical properties for a Chinese haze event measured during KORUS-AQ, *Atmos. Chem. Phys.*, 20, 6455-6478,  
813 <https://doi.org/10.5194/acp-20-6455-2020>, 2020.

814 Scarino, A. J., Obland, M. D., Fast, J. D., Burton, S. P., Ferrare, R. A., Hostetler, C. A., Berg, L. K., Lefer, B.,  
815 Haman, C., Hair, J. W., Rogers, R. R., Butler, C., Cook, A. L., and Harper, D. B.: Comparison of mixed layer  
816 heights from airborne high spectral resolution lidar, ground-based measurements, and the WRF-Chem model during  
817 CalNex and CARES, *Atmos. Chem. Phys.*, 14, 5547-5560, <https://doi.org/10.5194/acp-14-5547-2014>, 2014.

818 Sekiyama, T. T., Tanaka, T. Y., Shimizu, A., and Miyoshi, T.: Data assimilation of CALIPSO aerosol observations,  
819 *Atmos. Chem. Phys.*, 10, 39-49, <https://doi.org/10.5194/acp-10-39-2010>, 2010.

820 Seinfeld, J. H. and Pandis, S. N.: *Atmospheric Chemistry and Physics: From Air Pollution to Climate Change*, Third  
821 Edition, Ch. 8, John Wiley & Sons, New Jersey, 2016.

822 Shah, V., Jacob, D. J., Moch, J. M., Wang, X., and Zhai, S.: Global modeling of cloud water acidity, precipitation  
823 acidity, and acid inputs to ecosystems, *Atmos. Chem. Phys.*, 20, 12223-12245, <https://doi.org/10.5194/acp-20-12223-2020>, 2020.

824 [Su, T., Li, Z., and Kahn, R.: Relationships between the planetary boundary layer height and surface pollutants  
825 derived from lidar observations over China: regional pattern and influencing factors, \*Atmos. Chem. Phys.\*, 18,  
826 15921-15935, \[10.5194/acp-18-15921-2018\]\(https://doi.org/10.5194/acp-18-15921-2018\), 2018.](#)

827 [Sun, X., Yin, Y., Sun, Y., Sun, Y., Liu, W., and Han, Y.: Seasonal and vertical variations in aerosol distribution over  
828 Shijiazhuang, China, \*Atmos. Environ.\*, 81, 245-252, <https://doi.org/10.1016/j.atmosenv.2013.08.009>, 2013.](#)

829



830 Travis, K. R., Crawford, J. H., Nault, B. A., Kim, H., Jordan, C. E., Chen, G., Zhai, S., Wang, X., Jimenez, J. L.,  
831 Dibb, J. E., Brune, W. H., Weinheimer, A., Wennberg, P., Long, R., Szykman, J. J., Woo, J. H., Kim, Y., Li, K.,  
832 McDuffie, E., Luo, G., Zhang, Q., Kim, S.: Why do models have difficulty simulating ammonium nitrate and nitric  
833 acid in East Asia?, manuscript in preparation.

834 van Donkelaar, A., Martin Randall, V., Brauer, M., and Boys Brian, L.: Use of Satellite Observations for Long-  
835 Term Exposure Assessment of Global Concentrations of Fine Particulate Matter, *Environ. Health Perspect.*, 123,  
836 135-143, <https://doi.org/10.1289/ehp.1408646>, 2015.

837 van Donkelaar, A., Martin, R. V., Brauer, M., Hsu, N. C., Kahn, R. A., Levy, R. C., Lyapustin, A., Sayer, A. M., and  
838 Winker, D. M.: Global Estimates of Fine Particulate Matter using a Combined Geophysical-Statistical Method with  
839 Information from Satellites, Models, and Monitors, *Environ. Sci. Technol.*, 50, 3762-3772,  
840 <https://doi.org/10.1021/acs.est.5b05833>, 2016.

841 van der Werf, G. R., Randerson, J. T., Giglio, L., van Leeuwen, T. T., Chen, Y., Rogers, B. M., Mu, M., van Marle,  
842 M. J. E., Morton, D. C., Collatz, G. J., Yokelson, R. J., and Kasibhatla, P. S.: Global fire emissions estimates during  
843 1997–2016, *Earth Syst. Sci. Data*, 9, 697-720, <https://doi.org/10.5194/essd-9-697-2017>, 2017.

844 [van Donkelaar, A., Martin, R. V., Li, C., and Burnett, R. T.: Regional Estimates of Chemical Composition of Fine  
845 Particulate Matter Using a Combined Geoscience-Statistical Method with Information from Satellites, Models, and  
846 Monitors, \*Environ. Sci. Technol.\*, 53, 2595-2611, \[10.1021/acs.est.8b06392\]\(https://doi.org/10.1021/acs.est.8b06392\), 2019.](#)

847 [van Donkelaar, A., Martin, R. V., and Park, R. J.: Estimating ground-level PM2.5 using aerosol optical depth  
848 determined from satellite remote sensing, \*J. Geophys. Res. Atmos.\*, 111, \[10.1029/2005JD006996\]\(https://doi.org/10.1029/2005JD006996\), 2006.](#)

849 Wang, Q., Jacob, D. J., Fisher, J. A., Mao, J., Leibensperger, E. M., Carouge, C. C., Le Sager, P., Kondo, Y.,  
850 Jimenez, J. L., Cubison, M. J., and Doherty, S. J.: Sources of carbonaceous aerosols and deposited black carbon in  
851 the Arctic in winter-spring: implications for radiative forcing, *Atmos. Chem. Phys.*, 11, 12453-12473,  
852 <https://doi.org/10.5194/acp-11-12453-2011>, 2011.

853 Wang, Q., Jacob, D. J., Spackman, J. R., Perring, A. E., Schwarz, J. P., Moteki, N., Marais, E. A., Ge, C., Wang, J.,  
854 and Barrett, S. R. H.: Global budget and radiative forcing of black carbon aerosol: Constraints from pole-to-pole  
855 (HIPPO) observations across the Pacific, *J. Geophys. Res. Atmos.*, 119, 195-206,  
856 <https://doi.org/10.1002/2013JD020824>, 2014.

857 Wang, X., Heald, C. L., Ridley, D. A., Schwarz, J. P., Spackman, J. R., Perring, A. E., Coe, H., Liu, D., and Clarke,  
858 A. D.: Exploiting simultaneous observational constraints on mass and absorption to estimate the global direct  
859 radiative forcing of black carbon and brown carbon, *Atmos. Chem. Phys.*, 14, 10989-11010,  
860 <https://doi.org/10.5194/acp-14-10989-2014>, 2014.

861 Wang, Y., Zhang, Q., Jiang, J., Zhou, W., Wang, B., He, K., Duan, F., Zhang, Q., Philip, S., and Xie, Y.: Enhanced  
862 sulfate formation during China's severe winter haze episode in January 2013 missing from current models, *J.*  
863 *Geophys. Res. Atmos.*, 119, 4425-4440, <https://doi.org/10.1002/2013JD021426>, 2014.

864 Wei, J., Li, Z., Lyapustin, A., Sun, L., Peng, Y., Xue, W., Su, T., and Cribb, M.: Reconstructing 1-km-resolution  
865 high-quality PM<sub>2.5</sub> data records from 2000 to 2018 in China: spatiotemporal variations and policy implications,  
866 *Remote Sens. Environ.*, 252, 112136, <https://doi.org/10.1016/j.rse.2020.112136>, 2021.

867 Woo, J.-H., Kim, Y., Kim, H.-K., Choi, K.-C., Eum, J.-H., Lee, J.-B., Lim, J.-H., Kim, J., and Seong, M.:  
868 Development of the CREATE Inventory in Support of Integrated Climate and Air Quality Modeling for Asia,  
869 *Sustainability*, 12, 7930, <https://doi.org/10.3390/su12197930>, 2020.

870 [Xiao, Q., Chang, H. H., Geng, G., and Liu, Y.: An Ensemble Machine-Learning Model To Predict Historical PM<sub>2.5</sub>  
871 Concentrations in China from Satellite Data, \*Environ. Sci. Technol.\*, 52, 13260-13269, \[10.1021/acs.est.8b02917\]\(https://doi.org/10.1021/acs.est.8b02917\),  
872 2018.](#)

873 [Xu, J., Han, F., Li, M., Zhang, Z., Xiaohui, D., and Wei, P.: On the opposite seasonality of MODIS AOD and  
874 surface PM<sub>2.5</sub> over the Northern China plain, \*Atmos. Environ.\*, 215, 116909,  
875 <https://doi.org/10.1016/j.atmosenv.2019.116909>, 2019.](#)

876 [Xu, J. W., Martin, R. V., van Donkelaar, A., Kim, J., Choi, M., Zhang, Q., Geng, G., Liu, Y., Ma, Z., Huang, L.,  
877 Wang, Y., Chen, H., Che, H., Lin, P., and Lin, N.: Estimating ground-level PM2.5 in eastern China using aerosol](#)

878 [optical depth determined from the GOCI satellite instrument, Atmos. Chem. Phys., 15, 13133-13144, 10.5194/acp-](#)  
879 [15-13133-2015, 2015.](#)

880 [Xue, T., Zheng, Y., Tong, D., Zheng, B., Li, X., Zhu, T., and Zhang, Q.: Spatiotemporal continuous estimates of](#)  
881 [PM<sub>2.5</sub> concentrations in China, 2000–2016: A machine learning method with inputs from satellites, chemical](#)  
882 [transport model, and ground observations, Environ. Int., 123, 345-357, <https://doi.org/10.1016/j.envint.2018.11.075>,](#)  
883 [2019.](#)

884 Zhai, S., Jacob, D. J., Wang, X., Shen, L., Li, K., Zhang, Y., Gui, K., Zhao, T., and Liao, H.: Fine particulate matter  
885 (PM<sub>2.5</sub>) trends in China, 2013-2018: separating contributions from anthropogenic emissions and meteorology,  
886 Atmos. Chem. Phys., 19, 11031-11041 <https://doi.org/10.5194/acp-19-11031-2019>, 2019.

887 Zhai, S., Jacob, D. J., Wang, X., Liu, Z., Wen, T., Shah, V., Li, K., Moch, J. M., Bates, K. H., Song, S., Shen, L.,  
888 Zhang, Y., Luo, G., Yu, F., Sun, Y., Wang, L., Qi, M., Tao, J., Gui, K., Xu, H., Zhang, Q., Zhao, T., Wang, Y., Lee,  
889 H. C., Choi, H., and Liao, H.: Control of particulate nitrate air pollution in China, Nat. Geosci.,  
890 <https://doi.org/10.1038/s41561-021-00726-z>, 2021.

891 Zhang, L., Kok, J. F., Henze, D. K., Li, Q., and Zhao, C.: Improving simulations of fine dust surface concentrations  
892 over the western United States by optimizing the particle size distribution, Geophys. Res. Lett., 40, 3270-3275,  
893 <https://doi.org/10.1002/grl.50591>, 2013.

894 Zhang, L., Gong, S., Padro, J., and Barrie, L.: A size-segregated particle dry deposition scheme for an atmospheric  
895 aerosol module, Atmos. Environ., 35, 549-560, [https://doi.org/10.1016/S1352-2310\(00\)00326-5](https://doi.org/10.1016/S1352-2310(00)00326-5), 2001.

896 Zhang, X., Wang, H., Che, H.-Z., Tan, S.-C., Shi, G.-Y., and Yao, X.-P.: The impact of aerosol on MODIS cloud  
897 detection and property retrieval in seriously polluted East China, Sci. Total Environ., 711, 134634,  
898 <https://doi.org/10.1016/j.scitotenv.2019.134634>, 2020.

899 Zheng, B., Tong, D., Li, M., Liu, F., Hong, C., Geng, G., Li, H., Li, X., Peng, L., Qi, J., Yan, L., Zhang, Y., Zhao,  
900 H., Zheng, Y., He, K., and Zhang, Q.: Trends in China's anthropogenic emissions since 2010 as the consequence of  
901 clean air actions, Atmos. Chem. Phys., 18, 14095-14111, <https://doi.org/10.5194/acp-18-14095-2018>, 2018.

902 Ziemba, L. D., Lee Thornhill, K., Ferrare, R., Barrick, J., Beyersdorf, A. J., Chen, G., Crumeyrolle, S. N., Hair, J.,  
903 Hostetler, C., Hudgins, C., Obland, M., Rogers, R., Scarino, A. J., Winstead, E. L., and Anderson, B. E.: Airborne  
904 observations of aerosol extinction by in situ and remote-sensing techniques: Evaluation of particle hygroscopicity,  
905 Geophys. Res. Lett., 40, 417-422, <https://doi.org/10.1029/2012GL054428>, 2013.

906